Post-LGM glacial and geomorphic evolution of the Dora Baltea valley (western Italian Alps)

Elena Serra, Pierre Valla, Natacha Gribenski, Julien Carcaillet, Philip Deline

Quaternary Science Reviews 282 (2022) 107446

Contents lists available at ScienceDirect

Quaternary Science Reviews

journal homepage: www.elsevier.com/locate/quascirev

Post-LGM glacial and geomorphic evolution of the Dora Baltea valley (western Italian Alps)

Elena Serra [a, *], Pierre G. Valla [b], Natacha Gribenski [a], Julien Carcaillet [b], Philip Deline [c]

[a] Institute of Geological Sciences and Oeschger Centre for Climate Change Research, University of Bern, Baltzerstrasse 1-3 and Hochschulstrasse 4, CH-3012, Bern, Switzerland
[b] Institute of Earth Sciences (ISTerre), Université Grenoble Alpes, Université Savoie Mont Blanc, CNRS, IRD, IFSTAR, 38000, Grenoble, France
[c] EDYTEM, Université de Savoie, CNRS, 73000, Chambéry, France

ARTICLE INFO

Article history:
Received 21 May 2021
Received in revised form
22 February 2022
Accepted 26 February 2022
Available online xxx

Handling Editor: Giovanni Zanchetta

Keywords:
Post-LGM glacial history
Dora Baltea
Western European Alps
^{10}Be cosmogenic dating
Optically-stimulated luminescence dating
Ice surface reconstructions
ELA
Paraglacial processes

ABSTRACT

Paleoglacial reconstructions in the European Alps have mainly focused on specific climatic periods such as the Last Glacial Maximum (LGM) or the Younger Dryas, with few studies investigating post-LGM Alpine glacier fluctuations encompassing broader temporal periods. In this study, we present a detailed reconstruction of the post-LGM glacial history of the Dora Baltea catchment, which hosted one of the main Quaternary glacial systems of the western European Alps. By combining existing and new chronological constraints from glacial and postglacial landforms/deposits into 2D and 3D ice surface reconstructions, we quantitatively reproduce the timing and ice-configuration of six LGM to early Holocene paleoglacial stages. Our deglaciation sequence along the Dora Baltea valley can be correlated with specific Lateglacial to Holocene paleoclimatic periods, in line with post-LGM glacier reconstructions from other Alpine areas. We estimated paleo equilibrium-line altitudes (ELAs) for each ice stage, using empirical ice-geometric methods. Our results indicate a low ELA sensitivity to ice decay during the early stages of deglaciation, despite significant glacier retreat from the piedmont into the massifs, suggesting a major role of catchment topography in controlling ELA estimates of large glacial systems. Finally, we provide chronological constraints for two major valley-slope collapse events, both postdating the Dora Baltea glacier withdrawal but implying different landscape response time to deglaciation as well as different triggering factors.

1. Introduction

Fluctuations of mountain glaciers in response to modern or past climate variations have been widely recognized worldwide. Glacier mass-balance is highly sensitive to climate, with temperature and precipitation as main factors governing ice accumulation and ablation (e.g. Oerlemans, 2005; Mackintosh et al., 2017). For this reason, paleoglacier reconstructions and inferred fluctuations (i.e. advance/retreat) have often been investigated as first-order proxy for changes in paleoclimatic conditions (e.g. Kerschner and Ivy-Ochs, 2008; Davis et al., 2009). However, mountain glacier response to climate variations is modulated by additional factors (i.e. topography, debris cover, subglacial ice thermal regime and substrate etc.; Anderson and MacKintosh, 2012; Turrin et al., 2014; Lovell et al., 2015). There is therefore an increasing interest in investigating mountain glacier fluctuations under relatively known climate records (Federici et al., 2016; Wirsig et al., 2016b), in order to improve our understanding of glacier-climate interactions in alpine settings. Furthermore, slope processes are commonly recorded in formerly-glaciated valleys (e.g. Ivy-Ochs et al., 2017), but they can be associated to different forcings (glacial debuttressing, lithology, hydrological perturbation, earthquake; Cossart et al., 2008; McColl, 2012; Zerathe et al., 2014; Decaulne et al., 2016; Pánek et al., 2021). As a consequence, it appears critical to complement paleoglacier retreat sequences with records of post-glacial slope activity (Cossart et al., 2012; Schwartz et al., 2017), in order to further apprehend the post ice-retreat response of alpine landscapes.

In the European Alps, Late Pleistocene to Holocene climatic

Abbreviations: DB, Dora Baltea; LGM, Last Glacial Maximum; LIA, Little Ice Age; ELA, Equilibrium-Line Altitude; IMA, Ivrea Morainic Amphitheatre; KDE, Normal Kernel Density Estimate; THAR, Toe-to-Headwall Altitude Ratio; AAR, Accumulation Area Ratio; AABR, Area-Altitude Balance Ratio.

* Corresponding author.
E-mail address: elena.serra@geo.unibe.ch (E. Serra).

https://doi.org/10.1016/j.quascirev.2022.107446

variations have been reconstructed by combining multiple geomorphic and environmental records (e.g. lakes and peats, speleothems, and glacial records; Heiri et al., 2014b and references therein) with ice dynamics and atmospheric circulation models (Heiri et al., 2014a; Seguinot et al., 2018). The best quantitative constraints and paleoclimatic temporal sequences have been obtained for the period from the Last Glacial Maximum (LGM, 26.5–19.0 ka ago; Clark et al., 2009) to the Holocene (11.7 ka-present; Heiri et al., 2014b). Following the LGM, a general temperature warming trend, interrupted by short-term cooling episodes, has been recorded in the European Alps (Heiri et al., 2014b and references therein; Li et al., 2021), similar to Greenland ice-core records (Rasmussen et al., 2014). The overall temperature increase throughout the Lateglacial period (19.0–11.7 ka ago; Ivy-Ochs et al., 2007; Schmidt et al., 2012) was first suspended by climate deterioration probably associated to the Heinrich 1 ice-rafting event in the North Atlantic at 17.5–15.4 ka ago (Stanford et al., 2011). Afterwards, rapid warming (Von Grafenstein et al., 1999; Li et al., 2021) occurred during the Bølling-Allerød interstadial (14.6–12.8 ka; Heiri et al., 2014b) followed by abrupt cooling during the Younger Dryas (YD, 12.7–11.7 ka ago; Ivy-Ochs et al., 2007). The onset of the Holocene was characterized by warming conditions, punctuated by cold events such as the early Holocene Preboreal Oscillation (11.4–11.3 ka ago; Rasmussen et al., 2007) and the 8.2-ka event (Tinner and Lotter, 2001), evidenced in several Alpine records (e.g. Ilyashuk et al., 2011; Schimmelpfennig et al., 2012; Schindelwig et al., 2012; Nicolussi and Schlüchter, 2012). Between ca. 8 and 4.2 ka ago, Alpine paleoclimate proxies indicate relatively stable conditions similar to today, with only minor temperature oscillations (Ilyashuk et al., 2011; Affolter et al., 2019). Cool and wet conditions were re-established in the Neoglacial period, starting ca. 4.2 ka ago and culminating with the Little Ice Age (LIA, 1250–1860 CE; Le Roy et al., 2017 and reference therein). Paleoclimate proxies and ice/atmospheric numerical imulations provide additional information about Alpine paleo-precipitations, suggesting a shift in atmospheric circulation over the European Alps during the LGM, in addition to a general decrease in precipitation. Although the exact timing and magnitude of this shift are still uncertain, the modern northerly moisture advection from the Atlantic would have replaced dominant south-westerly precipitations from the Mediterranean Sea already before the YD (Florineth and Schlüchter, 2000; Luetscher et al., 2015; Becker et al., 2016; Monegato et al., 2017; Spagnolo and Ribolini, 2019; Rea et al., 2020; Baroni et al., 2021).

Paleoglacier responses to post-LGM climatic fluctuations have already been widely investigated in the European Alps (e.g. Böhlert et al., 2011; Cossart et al., 2012; Ivy-Ochs, 2015 and references therein; Chenet et al., 2016; Wirsig et al., 2016b, 2016a; Federici et al., 2016; Hofmann et al., 2019; Rolland et al., 2020). Based on mapping and dating of glacial landforms and deposits, several post-LGM ice-retreat and re-advance stages have been identified across the European Alps and tentatively related to the climatic periods. The so-called Alpine Lateglacial stadials (i.e. stages of ice stillstand or re-advance; Ivy-Ochs et al., 2007) hence include the Gschnitz stadial (~17–16 ka), in response to the Heinrich event 1 (e.g. Ivy-Ochs et al., 2006; Wirsig et al., 2016b), the Daun stadial (~14 ka; Ivy-Ochs, 2015), in response to a short interval of cooling within the Bølling-Allerød interstadial (Older Dryas or Aegelsee Oscillation, 14.0–13.9 ka; Lotter et al., 1992; Samartin et al., 2012; Li et al., 2021), and the Egesen stadial (~13.5–12.0 ka; Ivy-Ochs, 2015), in response to the YD cooling event (e.g. Federici et al., 2016; Boxleitner et al., 2019; Protin et al., 2019; Baroni et al., 2021). Alpine glaciers eventually retreated during the Holocene, following abrupt warming (Schimmelpfennig et al., 2012) and mostly remained within the LIA limits during Neoglacial ice re-advances (e.g. Porter and Orombelli, 1985; Holzhauser et al., 2005; Ivy-Ochs et al., 2009; Le Roy et al., 2017; Badino et al., 2018). Postglacial slope processes following deglaciation have also been documented during the Lateglacial and the Holocene (Cossart et al., 2008; Zerathe et al., 2014; Schwartz et al., 2017; Ivy-Ochs et al., 2017; Serra et al., 2021), although the causal links for valley slope-failure events have remained discussed (see details in Ivy-Ochs et al., 2017).

Due to the scarcity of continuous glacial deposits and landforms along Alpine valleys, only few studies have succeeded in providing detailed deglaciation sequences from LGM to LIA (Federici et al., 2016; Wirsig et al., 2016b). In the present study, we investigate the post-LGM glacial history of the Dora Baltea (DB) catchment (western Italian Alps; Fig. 1), one of the main glacial systems of the western European Alps. To this goal, we quantitatively reconstruct the timing and ice-configuration of several DB glacial stages, by combining existing and newly-acquired chronological constraints from glacial landforms and deposits into ArcGIS-based 3D ice-surface reconstructions. Moreover, we investigate the age of fluvio-lacustrine and slope-failure deposits along the DB valley to infer postglacial slope dynamics. Altogether, our results aim to assess the glacial and geomorphic responses of a large Alpine catchment to post-LGM climatic fluctuations.

2. Study area

2.1. The Dora Baltea catchment

This study focuses on the Dora Baltea (DB) catchment, a ~3400-km^2 drainage system located in the western Italian Alps (Fig. 1). The DB river flows for around 170 km NW-SE from the Mont Blanc massif to the Po Plain, and drains several tributary valleys characterised by the presence of major 4000-m Alpine peaks (e.g. Mont Blanc, Monte Rosa, Matterhorn and Gran Paradiso). The geology of the DB catchment is complex, with the main structural domains of the Alpine range (Vezzoli et al., 2004; Dal Piaz et al., 2008; Perello et al., 2008; Polino et al., 2008). Bedrocks belonging to the Helvetic-Ultrahelvetic zone outcrop in the Mont Blanc area, composed of the typical granite of the Mont Blanc external massif and its sedimentary cover. Moving eastwards, Penninic units of increasing metamorphic grade occur: Briançonnais metasedimentary rocks (e.g. between Mont Blanc and Matterhorn), crystalline bedrocks of internal massifs (e.g. Gran Paradiso and Monte Rosa), Piemonte zone ophiolitic units (e.g. Matterhorn area). Austroalpine metamorphic rocks outcrop in the central (e.g. NE of Aosta) and eastern (e.g. SW and NE of Donnas) sectors of the DB catchment.

Temperate climatic conditions prevail in the DB basin (present-day mean annual temperature ranges from −10° to 15 °C; Regione Autonoma Valle d'Aosta, 2009). Modern observations indicate a moderate spatial variability in precipitation across the DB catchment (Isotta et al., 2014; Mey et al., 2016), with higher precipitation (~1800 mm/yr at around 4000 m a.s.l.) in the Mont Blanc massif compared to the north-western and southern sectors of the DB catchment (~1400 mm/yr for Matterhorn and Monte Rosa area, and ~1150 mm/yr in the Grand Paradiso, at around 4000 m a.s.l.), while semi-arid conditions prevail in the central part of the DB valley floor (400–500 mm/yr, between Verbion and Saint Pierre, at around 800 m a.s.l.; Fig. 1). Modern glaciers cover an area of 119.6 km^2 (3.6% of the DB catchment) and are of limited size (<10% glaciers are larger than 1 km^2) with terminus elevations ranging from 2601 to 2800 m a.s.l. in DB tributary valleys (data from 2005; Diolaiuti et al., 2012). The most recent mean Equilibrium-Line Altitude (ELA) estimate is 3015 ± 197 m a.s.l. for the entire DB catchment (data from 1975; Vanuzzo, 2001).

During the Quaternary, the extensive DB glacial system fluctuated repeatedly from the internal catchment down to ~20 km into

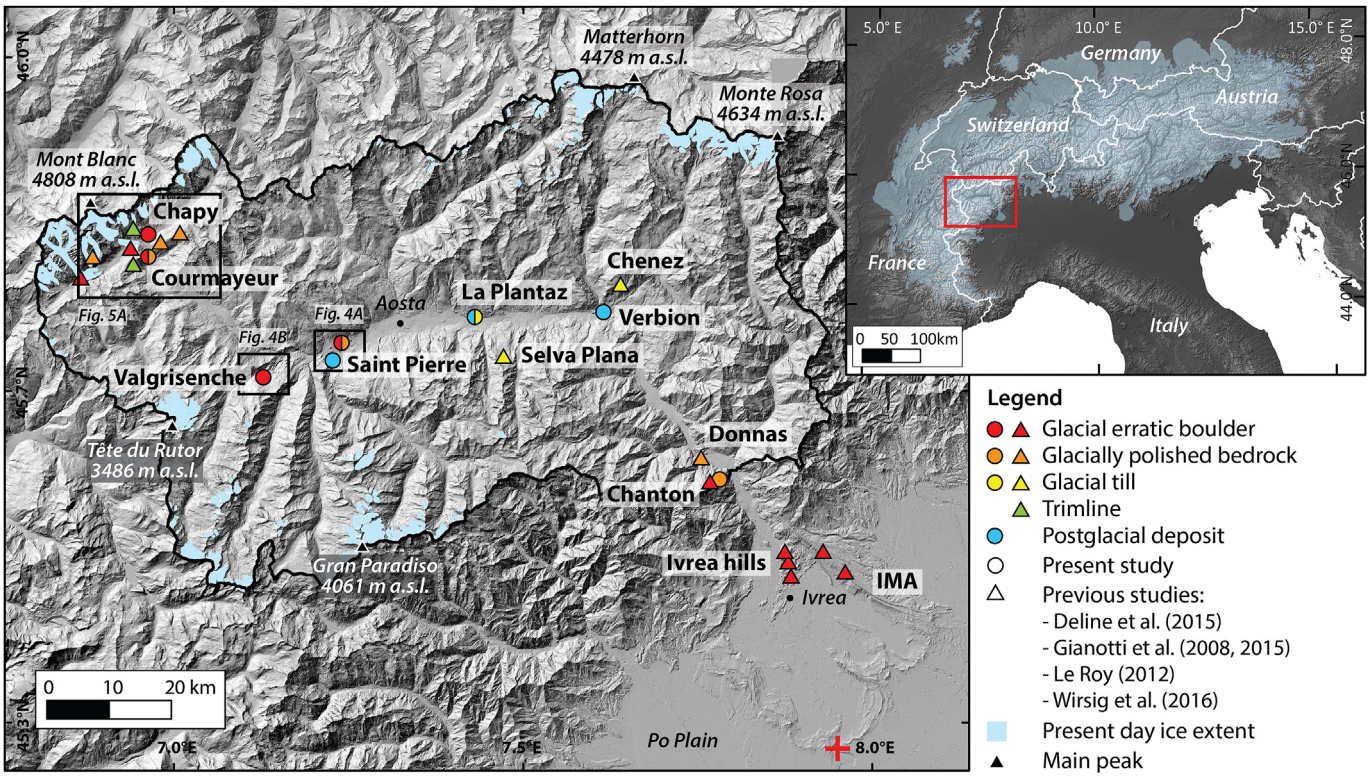

Fig. 1. Study area, with (post-)glacial landforms/deposits (DEM from Regione Piemonte and Regione Autonoma Valle d'Aosta). In bold are the investigated sites, in italic some toponyms within the DB valley. Symbol colours (circles: this study, triangles: literature) correspond to the five investigated geomorphological categories. Present-day glaciers (light blue, GlaRiskAlp Project, http://www.glariskalp.eu) and main topographic peaks are indicated. Black lines mark the extent of the DB catchment within the mountain front. IMA: Ivrea Morainic Amphitheatre (red cross indicates the location where the DB river crosses the IMA). Black boxes highlight locations of enlargements shown in Fig. 4A, B, and 5A. Top-right inset shows location of the DB catchment (red open box) within the European Alps, with the LGM ice extent (light blue; Ehlers and Gibbard, 2004) and the national borders (white lines). (For interpretation of the references to colour in this figure legend, the reader is referred to the Web version of this article.)

the Po plain (Gianotti et al., 2008, 2015), building the Ivrea morainic amphitheatre (IMA; Fig. 1), one of the largest in Europe. While the most external ridges formed during the Early Pleistocene (based on paleomagnetic data; Carraro et al., 1991), the DB glacier lastly reached the IMA during the LGM (Gianotti et al., 2008, 2015). Post-LGM ice retreat occurred progressively, with the DB glacier persisting and oscillating within the IMA until ca. 19 ka (^{10}Be surface-exposure ages; Gianotti et al., 2008, 2015; Fig. 1). During the Lateglacial, the DB glacier retreated behind the mountain front into the upper catchment, with several non-dated stages of glacier halt or re-advance (i.e. stadials), as testified by glacial landforms and sediment deposits identified along the DB valley (Gianotti et al., 2008, 2015).

Radiometric chronology for the DB glacier history has focused on the (pre-)LGM maximum extent (IMA; Gianotti et al., 2008; 2015) and only sparse chronological data exist for the post-LGM glacial history: Lateglacial ice-surface lowering in the Mont Blanc massif (Wirsig et al., 2016a), and YD glacier re-advances in the Gran Paradiso massif (Baroni et al., 2021). In addition, Holocene glacial extents have been constrained in the Mont Blanc massif (Le Roy, 2012; Deline et al., 2015) and for the Rutor Glacier (Porter and Orombelli, 1985; Badino et al., 2018, Fig. 1). However, no chronological constraint was so far available for any Lateglacial stadial along the main DB valley, preventing to establish a continuous deglaciation sequence for the DB glacial system. In this study, we aim to fill this spatial and temporal gap by providing new chronological data and ice-geometry reconstructions for the DB Lateglacial stadials.

2.2. Key sites for glacial reconstructions

Along the DB valley, we identified locations with potential significance for Lateglacial stadials and postglacial slope processes (Fig. 1), by combining existing literature constraints with geomorphological mapping (field investigations and remote-sensing mapping based on the high-resolution DEMs and orthophotos from Regione Piemonte and Regione Autonoma Valle d'Aosta). We classified the identified landforms and deposits in five categories (Fig. 1 and Table S1), each providing different constraints for paleoglacier reconstructions or postglacial slope dynamics. Glacial erratic boulders and glacially-polished bedrocks give information about the glacier position in a deglaciation sequence. (1) In the case of boulders located on moraine ridges, more precise information about the glacier frontal position (i.e. frontal moraine) or thickness (i.e. lateral moraine) during a phase of ice re-advance/stillstand can be obtained, since moraines are assumed to be built during stages of ice re-advance/stillstand (Kirkbride and Winkler, 2012; Lukas, 2012). Distinction between ice re-advance or stillstand would require detailed sedimentological investigations which are outside of the scope of the present study, due to the scale of the study area and the lack of sediment outcrops for investigated sites. (2) Erratic boulder fields and polished bedrocks instead provide timing constraints for ice retreat and thinning (when located along the valley side), as they are interpreted to be respectively deposited and exposed during ice withdrawal. (3) Glacial tills along the valley slopes provide information on both the glacier position and minimum thickness, as inferred to derive from debris transported and deposited at the base/margin of the ice. (4) Trimlines (i.e.

geomorphic transition between frost-weathered zone above and glacially-polished surface below) are assumed to represent the LGM ice-surface elevation (Coutterand and Buoncristiani, 2006; Wirsig et al., 2016a). (5) Rockslide, landslide, glacio-fluvial and fluviolacustrine deposits, are indicative of postglacial slope activity and thus provide a minimum time constraint for glacier retreat.

In the piedmont area (easternmost sector; Fig. 1), we considered literature constraints (sites previously dated by Gianotti et al., 2008, 2015; Fig. S1) from glacial erratic boulders on an internal IMA morainic ridge (indicative of glacier terminal position during the LGM), and erratics on the Ivrea hills (tracing the early glacier retreat from the IMA). Moving upstream from the IMA, three additional sites were retained closely behind the mountain front: (1) the 1-km long Chanton lateral moraine and boulders (DB valley right side, around 1000 m above the present-day valley floor; described in Gianotti and Forno, 2017 but undated), testifying ice surface elevation, (2) two glacially-polished bedrock surfaces ~100–200 m below the Chanton moraine (undated by previous studies), documenting glacier thinning, and (3) a glacially-polished bedrock surface along the DB valley floor at Donnas, marking ice-front retreat (dated by Gianotti et al., 2008, 2015; Fig. S1). In the mid-catchment, a fluviolacustrine deposit was investigated in Verbion (DB valley left side, 20–60 m above the present-day valley floor; undated by previous studies; Fig. 2A), and characterised by a succession of laminated silt, turbiditic sand and gravel lenses previously interpreted as being deposited within a rockslide-dammed lake (Mont Avi rockslide, DB right valley side, downstream of Verbion; described in Giardino, 2005a but undated). Till deposits without age constraint were identified on the DB valley slopes at Chenez and Selva Plana, around 1200–1300 m above the present-day valley floor (Dal Piaz et al., 2008, Fig. 1), and at a much lower elevation (50 m above the valley floor) in La Plantaz (Fig. 1). Fluvioglacial sediments (gravel, sandy and silty strata laying on top of lodgment till) were also identified in the investigated section of La Plantaz (Fig. 2C), previously interpreted as ice-margin contact deposits (i.e. kame terrace) deformed by short-term ice margin oscillations during the retreat of the DB glacier (Giardino, 2005b; undated by previous studies).

Saint Pierre location (Fig. 1) is a key site for investigating the connection between the DB glacier and its tributaries from the Gran Paradiso massif. In this area, both glacial and postglacial deposits were investigated. Granitic erratic boulders and a polished bedrock surface were identified on the Saint Pierre bedrock hill (showing glacial lineaments, Figs. 3A and 4A), testifying ice-front retreat. Few kilometers upstream, we mapped a prominent (2-km long) lateral moraine with micaschist boulders at the entrance of Valgrisenche (tributary valley from Gran Paradiso massif; Fig. 4B). Finally, opposite side of Saint Pierre hill, we identified boulders with gneissic lithologies (Fig. 4A) with proposed rockslide origin. Nearby this site, at the confluence between the DB river and Grand Eyvia tributary (Fig. 4A), a fluviolacustrine succession (clayey, silty and sandy layers) capping a rockslide deposit (diamicton; Fig. 2B) was logged. This succession was previously related to early Holocene valley damming by slope failure (Nicoud et al., 1999).

Lastly, in the uppper DB catchment close to Courmayeur (Fig. 1), several key sites with a rich record of paleoglacial landforms/deposits were considered in this study. Trimlines and high-elevation glacially-polished bedrocks were previously investigated in Val Veny and Val Ferret (Porter and Orombelli, 1982; Coutterand and Buoncristiani, 2006; Wirsig et al., 2016a, Figs. 3B and 5A). Erratic boulders were identified on two lateral moraines at Courmayeur, with a polished bedrock knob between them (right side of the DB river; Fig. 3B and C, 5A and B; undated by previous studies). Upstream of Courmayeur, erratic boulders and lateral moraine ridges have also been reported in the literature for the Val Veny (dated by Le Roy, 2012, and Deline et al., 2015, Fig. 5A), as well as for the Val Ferret (Porter and Orombelli, 1982; undated) where we investigated a small morainic ridge (Chapy; Figs. 3D and 5C).

When not already available in the literature, geochronological constraints of the above-mentioned landforms and deposits were obtained in this study, using ^{10}Be surface-exposure (erratic and rockslide-transported boulders, polished bedrocks) and optically-stimulated luminescence burial (fluvioglacial and fluviolacustrine deposits) dating. Temporal and spatial distributions of the investigated landforms/deposits were then used to (1) reconstruct the evolution of the DB paleo-glacier from the LGM to the early Holocene, as well as to (2) assess postglacial slope dynamics along the DB valley.

3. Methods

3.1. Geochronology

3.1.1. ^{10}Be surface-exposure dating

Eighteen erratic/rockslide-transported boulders and four glacially-polished bedrocks were sampled for ^{10}Be surface-exposure dating in four sites (Table 1, Figs. 1, 4 and 5). At the entrance of the DB valley, two micaschist polished bedrocks were sampled below the Chanton moraine (CHAN20_04 and 05; Fig. S1). In the area of Saint Pierre (Fig. 4), five granitic erratic boulders (STP19_01, 03, 04, 05, 06) and one quartz vein from calcschist polished bedrock (STP19_02) were sampled on Saint Pierre hill (Fig. 4A). In addition, we collected two gneissic rockslide-transported boulders (POY19_01 and 02) on the DB valley right flank (3 km south of Saint Pierre hill; Fig. 4A), and two micaschist boulders from Valgrisenche lateral moraine (upstream of Saint Pierre, VGRI19_01, 02; Fig. 4B). Close to Courmayeur, six granitic boulders on top of the two lateral morainic ridges (VIL18_02, 03, 04, 06, 08, 09) and one polished bedrock knob (VIL18_01) were investigated (Fig. 5B). Lastly, three erratic boulders (CHA_01, 02, 03) were sampled on the Chapy moraine (Fig. 5C).

Samples were collected with saw, hammer and chisel from flat surfaces on top of the boulders (minimum 1-m height) and in the middle of polished bedrock outcrops. Sampled surfaces with apparent minimal erosion and absence of soil coverage were chosen (Gosse and Phillips, 2001). Samples were crushed and sieved to isolate the 250–400 μm grainsize fraction. Modified procedures based on Kohl and Nishiizumi (1992) were followed to isolate pure quartz (Institute of Geological Sciences - University of Bern, Switzerland). ^{10}Be extraction was completed by adapting conventional chemical treatments from Brown et al. (1991) and Merchel and Herpers (1999) (GTC platform, ISTerre, - University Grenoble Alpes, France). Measurements of ^{10}Be/^{9}Be ratios were performed at ASTER French National AMS facility (CEREGE, Aix-en-Provence, France; Arnold et al., 2010) and calibrated against the in-house Be standard (^{10}Be/^{9}Be ratio 1.191 $\times$ 10^{11}; Braucher et al., 2015). Calculated ^{10}Be concentrations (Table 1) were corrected for full process blank ^{10}Be/^{9}Be ratios (see details in Table 1).

Calculation of ^{10}Be surface-exposure ages were performed with the online CREp program (Martin et al., 2017; https://crep.otelo.univ-lorraine.fr/#/init). We also re-calculated ^{10}Be surface-exposure data from the literature (Gianotti et al., 2008, 2015; Le Roy, 2012; Deline et al., 2015; Wirsig et al., 2016a; see Figs. 1 and 5A and S1 for locations and Table S3 for details). We used a ^{10}Be production rate by neutron spallation at sea-level and high-latitude (SLHL) of 4.16 ± 0.10 at g^{-1} a^{-1} (from the Chironico landslide, southern Swiss Alps, closest calibration site to our study area; Claude et al., 2014), scaled at the sampling sites based on the LSDn scaling scheme (Lifton et al., 2014). This scaling scheme integrates corrections for atmospheric pressure and geomagnetic field

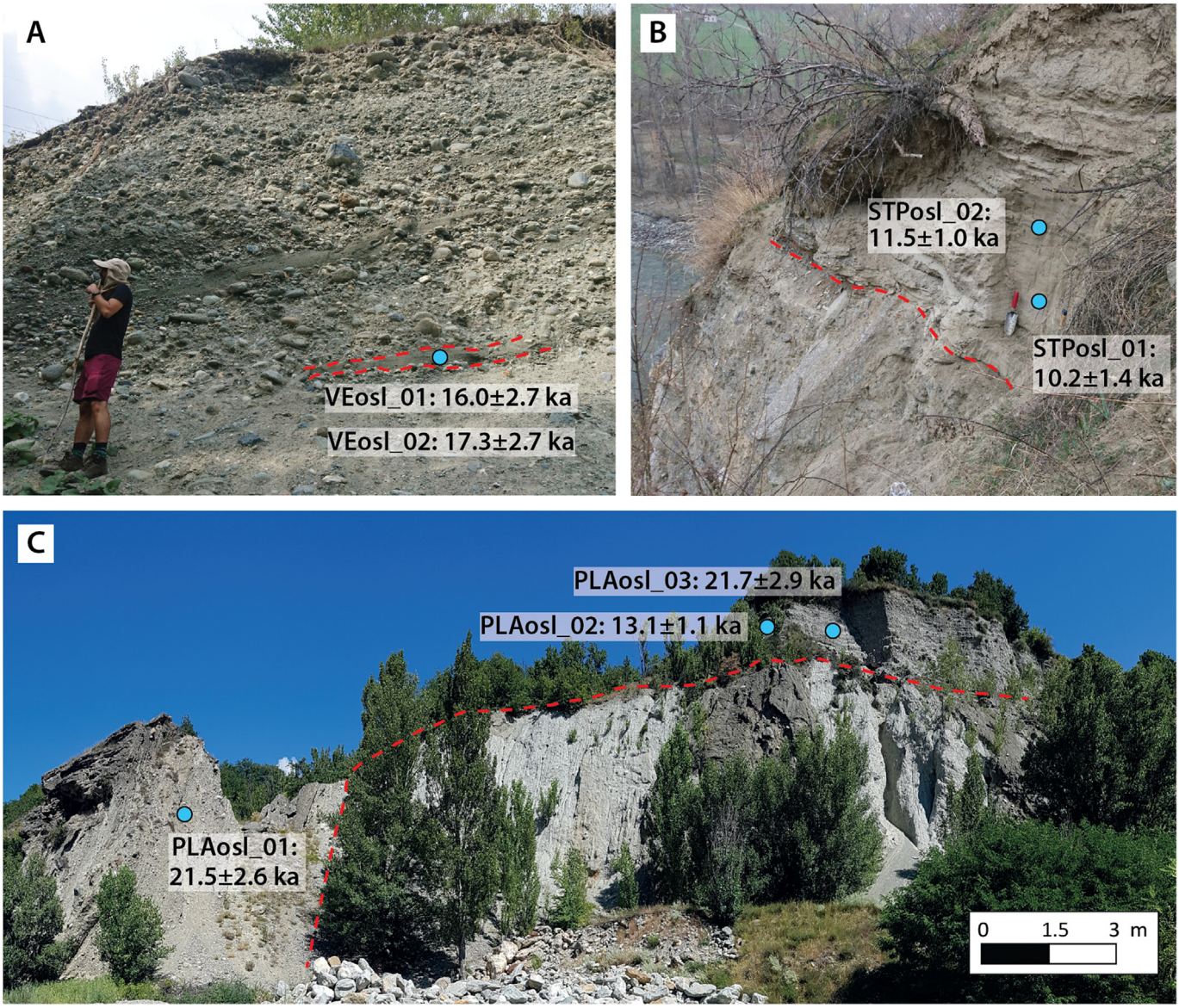

Fig. 2. Luminescence dating sites with field photographs and output feldspar IR_{50} burial ages (see Fig. 1 for locations within the DB catchment). Colored dots indicate the sample locations. More detailed pictures of each outcrop are reported in the Supplementary Material (Figs. S2, S3 and S4). **A)** Outcrop of gravel- and sandy-inclined layers from the Verbion fluviolacustrine deposit. Red dashed lines enlcose the ~15-cm thick sandy layer (VEosl_01). For indication, the age of nearby sample VEosl_02 (sampling site not visble on this picture, see Fig. S2) is also shown. **B)** Outcrop of Saint Pierre rockslide deposit (below the red dashed line) and fluviolacustrine sediments (STPosl_01 and 02, above the red dashed line). **C)** Fluvioglacial sedimentary sections of La Plantaz, interpreted as kame terrace deposits. The red dashed line defines the unconformity between the lodgement till at the base and the fluvioglacial strata on top. The folding of the fluvioglacial strata due to ice contact deformation is visible: from subhorizontal in the top right corner of the picture (samples PLAosl_02 and 03) to strongly inclined (70°, N 210°) on the left (PLAosl_01). (For interpretation of the references to colour in this figure legend, the reader is referred to the Web version of this article.)

fluctuations according to the ERA-40 reanalysis data set (Uppala et al., 2005) and the Lifton-VDM2016 geomagnetic database (Lifton, 2016). Topographic shielding corrections based on field measurements were used in the calculations (Dunne et al., 1999). An estimated erosion rate of 0.1 mm ka^{-1} was applied for ^{10}Be age correction (André, 2002; Deline et al., 2015; Wirsig et al., 2016a). Although temporal and spatial variability in snow accumulation is likely across the DB catchment, it is challenging to estimate. We thus chose to maintain a uniform approach for the entire ^{10}Be age dataset, and did not apply any snow correction. Hence, the ^{10}Be calculated ages need to be considered as minimum exposure ages.

In order to provide chronological constraints for each landform/deposit, we first assessed the degree of clustering of the individual ^{10}Be ages. Normal kernel density estimate (KDE) of the individual ages were graphically represented (modified code for synthetic probability ideograms from https://depts.washington.edu/cosmolab/pubs/gb_pubs/camelplot.m, based on Lowell, 1995). Sets of ^{10}Be ages for each landform were then categorized as well-clustered or poorly-clustered, based on visual assessment. Individual ages were sometimes considered as outliers and discarded, based on the geomorphological and stratigraphic contexts (see details and discussion in section 4.1.1). For well-clustered datasets, individual age KDE were summed (Lowell, 1995) and the mode and standard deviation of the summed KDE were considered as the landform/deposit age with its respective error (because of the skewness of the summed KDE, asymmetric errors were obtained).

Fig. 3. Field photographs of paleoglacial landforms and deposits sampled for ^{10}Be surface-exposure dating (see Figs. 1, 4 and 5 for locations within the DB catchment). **A)** Granitic erratic boulder (STP19_01) located on the Saint Pierre hill. **B)** View from Courmayeur towards the confluence of Val Veny and Val Ferret. VIL18_01 indicates the polished bedrock knob located between the two morainic ridges, and Cou6-9 show the steep bedrock cliff above. **C)** Granitic erratic boulder (VIL18_02) sampled on the external moraine of Courmayeur. **D)** Granitic erratic boulder (CHA19_01) sampled on the Chapy morainic ridge in Val Ferret (upstream of Courmayeur).

For landforms with poorly-clustered datasets, individual ages were considered separately when interpreting the landform/deposit age.

3.1.2. Optically-stimulated luminescence dating

Seven sandy samples were collected for luminescence burial dating from the fluviolacustrine and fluvioglacial deposits of Verbion (VEosl_01 and 02; Figs. 2A and S2), La Plantaz (PLAosl_01, 02 and 03; Figs. 2C and S3), and Saint Pierre (STPosl_01 and 02; Figs. 2B and S4). Samples were collected in black plastic tubes and prepared under subdued laboratory light, following standard procedures (preparation details in Lowick et al., 2015). Quartz and feldspar minerals from coarse grain fraction (100–250 μm depending on samples) were isolated, however, due to the dim luminescence signal and high feldspar contamination revealed by preliminary measurements, quartz separates were not used for further analysis. Feldspar luminescence measurements were conducted using both small (1-mm) aliquots and single-grain discs in order to better assess potential heterogeneous bleaching (i.e. incomplete resetting of luminescence signal before deposition), common in paraglacial deposits (Duller, 2008; Smedley et al., 2016).

All luminescence measurements were performed using a Risø TL/OSLDA-20 equipped with a calibrated ^{90}Sr/^{90}Y beta source and a single-grain attachment (Bøtter-Jensen, 1997; Institute of Geological Sciences - University of Bern, Switzerland). Feldspar infrared stimulation of small aliquots was performed with IR LEDs emitting at 875 nm. For single-grain measurements, a 140 mW IR laser emitting at 830 nm fitted with a RG-780 filter was used (Bøtter-Jensen, 1997). Infrared-stimulated luminescence (IRSL) signals were detected in the blue wavelength through a Schott BG-39 and L.O.T.-Oriel D410/30 nm filter combination. Small-aliquot and single-grain feldspar equivalent doses (D_e) were measured using post-IR IRSL protocols (Buylaert et al., 2009; Reimann and Tsukamoto, 2012). For samples VEosl_01–02 and STPosl_01–02, a $pIRIR_{225}$ protocol was applied (Buylaert et al., 2009; Tabs. S4A and C). For samples PLAosl_01, 02 and 03 (PLAosl_02 only small-aliquot measurements), D_e estimates were determined with a $pIRIR_{150}$ protocol (Table S4B), in order to minimize thermal transfer processes (Reimann and Tsukamoto, 2012).

Because of its better bleaching properties (Colarossi et al., 2015), the IR_{50} signal was used for final age determination. Small-aliquot and single-grain IR_{50} D_e distributions were analysed using the Central Age Model (CAM; Galbraith et al., 1999) or, in case of partial bleaching diagnosis, using the Finite Mixture Model (FMM; Galbraith and Green, 1990). Significant partial bleaching was considered in case of (1) large discrepancy between the small-aliquot and single-grain D_e estimates, and (2) differences between IR_{50} and $pIRIR_{225}$/$pIRIR_{150}$ D_e estimates, (3) widely-spread and multimodal D_e distributions (overdispersion OD>20% for small aliquots and OD>30% for single-grain discs; Galbraith and Roberts, 2012; Gaar et al., 2019). The FMM was run with sigma-b values (σ_b; equivalent to expected OD for a well-bleached sample) of 0.2 for small aliquots and 0.3 for single-grain discs (Gaar et al., 2019; Gribenski et al., 2018).

U, Th and K concentrations (Table 2) of bulk sediment were measured using high-resolution gamma spectrometry (Department of Chemistry and Biochemistry - University of Bern, Switzerland; Preusser and Kasper, 2001) and were input in the Dose Rate and Age Calculator (DRAC; Durcan et al., 2015) for dose rate determination (Table 2). Fading measurements (g_{2days}) were conducted for each individual sample on small aliquots (3–10 per sample) previously-used for D_e measurements (Auclair et al., 2003; Kreutzer and Burow, 2020). Fading correction was performed according to Huntley and Lamothe (2011) for both small aliquots and single-grain discs FMM or CAM D_e estimates with the

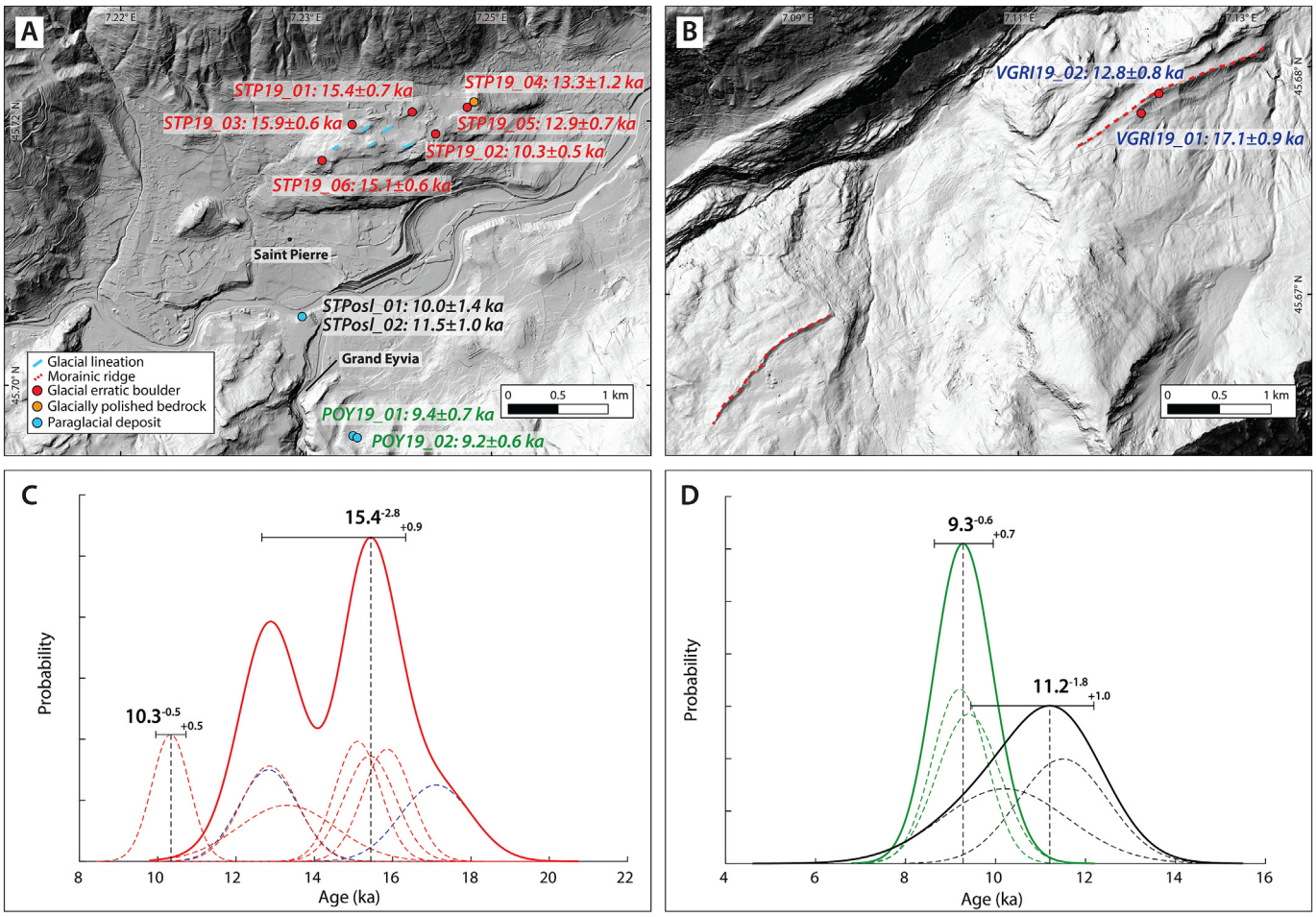

Fig. 4. ^{10}Be surface-exposure (color) and luminescence (black) ages from Saint Pierre and Valgrisenche sites (locations in Fig. 1; modified DEM from Regione Autonoma Valle d'Aosta). **A)** Sample location and ^{10}Be surface-exposure ages of erratic boulders and glacially-polished bedrock on Saint Pierre hill. At the outlet of the Grand Eyvia tributary, ^{10}Be surface-exposure ages of rockfall-derived boulders and luminescence ages of fluviolacustrine sediments are shown. **B)** Sample location and ^{10}Be surface-exposure ages of the two erratic boulders sampled on the lateral moraine of Valgrisenche. **C)** Individual (dashed lines) and summed (red continuous line) KDE of ^{10}Be surface-exposure ages from Saint Pierre hill erratics and polished bedrock (red dashed lines) and from Valgrisenche erratics (blue dashed lines). Only sample STP19_02 was excluded as outlier from the summed KDE (see text for details). The mode and uncertainties of the summed KDE are reported. **D)** Individual (dashed lines) and summed (continuous lines) KDE of ^{10}Be surface-exposure and luminescence ages of postglacial samples at the outlet of Grand Eyvia tributary (rockfall-derived boulders in green, fluviolacustrine sediments in black). Modes and uncertainties of the summed KDE are reported. (For interpretation of the references to colour in this figure legend, the reader is referred to the Web version of this article.)

Luminescence R package (Kreutzer, 2020) before final age calculation (Table 2). Finally, the same approach as for ^{10}Be surface-exposure ages was applied for deriving deposit ages: sample individual age KDEs were summed, when possible, and the mode and standard deviation of the summed KDE were calculated (see section 3.1.1 for details).

3.2. Paleoglacial reconstructions and equilibrium-line altitude (ELA) calculations

Following the identification of distinct paleoglacial stages within the DB catchment, ice-surface 3D geometry was reconstructed for each stage, using a semi-automatic ArcGIS routine, similar to the approach of the GlaRe ArcGIS toolbox (Pellitero et al., 2016).

First, key landforms and deposits within the DB catchment (Fig. 1 and Table S1) were grouped to define distinct stages of ice retreat or stillstand/re-advance, based on their radiometric age (^{10}Be surface-exposure and luminescence burial dating), spatial distribution and geomorphological significance. Second, for each defined ice-front position, 2D ice-surface profiles were generated using the Excel™ spreadsheet program *Profiler v.2* (Benn and Hulton, 2010), which is based on a steady-state solution of a 'perfectly plastic' ice model. We propagated the 2D ice profiles into the DB valley and its major tributaries, using as ice-front and ice-surface constraints the identified landforms/deposits grouped into the same paleoglacial stage (Fig. 6, Table S1). Present-day topography along the main hydrographic channels was used as input for glacier bed topography (Fig. 6A). Shape-factor (f) values were calculated along the DB valley and its tributaries as input in the *Profiler v.2* model, in order to include the valley side-drag effects on ice thickness (Benn and Hulton, 2010). We calculated f according to Eq. (12) from Benn and Hulton (2010) for a total of 62 cross-sections (13 in DB valley and 49 in tributaries; Fig. 6A). Between each cross-section, f values along the main flow line were computed by linear interpolation at 25-m interval. The *Profiler v.2* model was run with glacier basal shear stress (τ) values varying between 50 and 100 kPa, selected according to the literature (Cuffey and Paterson, 2010; Pellitero et al., 2016) and from best-fitting approach between the modelled ice surface and our ice-surface geomorphological constraints (Pellitero et al., 2016, Fig. 6B; Table S1). We obtained 3D ice surfaces for individual

Table 1
^{10}Be surface-exposure dating for samples collected in the present study. Samples are listed moving upstream from the IMA. Sample locations, topographic shielding,^{10}Be/^{9}Be blank corrected ratios,^{10}Be concentrations and exposure ages are reported. Sample density is assumed to be 2.65 g cm^{-3} for all samples. Mass of quartz dissolved, mass of Be carrier and non-blank corrected^{10}Be/^{9}Be ratios are reported in Table S2.

Sample Name	Location WGS 84 (°N/°E)	Elevation (m a.s.l.)	Topographic shielding [a]	Sample thickness (cm)	^{10}Be/^{9}Be blank corrected (10^{-14} at g^{-1}) [b]	^{10}Be/^{9}Be uncertainty (%)	^{10}Be concentration (10^{5} at g^{-1})	^{10}Be exposure age (ka) [c]
CHAN20_04	45.5792/7.7809	1134	0.990	2.5	8.86	3.24	1.49 ± 0.05	14.6 ± 0.6
CHAN20_05	45.5814/7.7800	1043	0.985	2.5	11.1	8.55	1.81 ± 0.15	19.0 ± 1.6
STP19_01	45.7172/7.2428	830	0.989	3.0	7.23	3.63	1.22 ± 0.05	15.4 ± 0.7
STP19_02	45.7158/7.2450	815	0.991	3.0	4.85	4.03	0.80 ± 0.03	10.3 ± 0.5
STP19_03	45.7163/7.2374	845	0.990	3.0	7.67	3.14	1.27 ± 0.04	15.9 ± 0.6
STP19_04	45.7181/7.2486	786	0.990	3.0	3.30	9.10	1.01 ± 0.09	13.3 ± 1.2
STP19_05	45.7178/7.2483	793	0.985	3.0	5.87	5.17	0.97 ± 0.05	12.9 ± 0.7
STP19_06	45.7142/7.2347	862	0.988	3.0	7.30	3.12	1.23 ± 0.04	15.1 ± 0.6
POY19_01	45.6953/7.2381	811	0.980	2.5	4.32	6.96	0.71 ± 0.05	9.4 ± 0.7
POY19_02	45.6953/7.2378	810	0.979	2.5	2.30	5.78	0.70 ± 0.04	9.2 ± 0.6
VGRI19_01	45.6777/7.1241	1601	0.984	3.0	13.17	4.94	2.65 ± 0.13	17.1 ± 0.9
VGRI19_02	45.6789/7.1259	1559	0.976	3.0	12.13	5.46	1.83 ± 0.10	12.8 ± 0.8
VIL18_01	45.7969/6.9649	1242	0.924	3.0	7.21	3.64	1.48 ± 0.06	14.2 ± 0.6
VIL18_02	45.7974/6.9644	1248	0.947	3.0	11.70	3.34	1.55 ± 0.05	14.4 ± 0.6
VIL18_03	45.7979/6.9643	1255	0.906	4.5	10.77	3.57	1.36 ± 0.05	13.3 ± 0.6
VIL18_04	45.7990/6.9643	1277	0.920	4.0	11.1	3.80	1.48 ± 0.06	14.0 ± 0.6
VIL18_06	45.7992/6.9646	1281	0.936	5.0	7.09	3.35	0.92 ± 0.03	8.6 ± 0.4
VIL18_08	45.7985/6.9650	1272	0.918	6.0	9.60	3.31	1.22 ± 0.04	11.8 ± 0.5
VIL18_09	45.7977/6.9653	1261	0.939	5.0	6.05	10.31	0.78 ± 0.08	7.4 ± 0.7
CHAP19_01	45.8225/6.9667	1458	0.966	2.5	2.38	7.68	0.40 ± 0.03	3.2 ± 0.3
CHAP19_02	45.8217/6.9665	1439	0.964	2.5	2.24	2.80	0.32 ± 0.02	2.6 ± 0.2
CHAP19_03	45.8216/6.9666	1432	0.964	2.5	1.60	2.15	0.24 ± 0.03	1.9 ± 0.3

[a] Topographic shielding correction according to Dunne et al. (1999).
[b] ^{10}Be/^{9}Be ratios of batch-specific analytical blanks used for the correction are 6.3 ± 0.7 × 10^{-15} (CHAN samples), 5.4 ± 0.6 × 10^{-15} (VIL samples), 6.2 ± 0.6 × 10^{-15} (POY19_01 and STP samples except STP19_04), 5.9 ± 0.6 × 10^{-15} (STP19_04, POY19_02), and 5.5 ± 1.0 × 10^{-15} (VGRI and CHAP samples).
[c] Ages are reported with external uncertainties (i.e. including both analytical errors and production-rate uncertainties). Ages were calculated with a SLHL^{10}Be production rate of 4.16 ± 0.10 at g^{-1} a^{-1} (Claude et al., 2014) and LSDn scaling scheme (Lifton et al., 2014) and considering an estimated surface erosion rate of 0.1 mm ka^{-1} (André, 2002). No snow-cover correction was applied.

Table 2
Details of luminescence dating on single grains (all samples except PLAosl_02) and small-aliquots (PLAosl_02), using feldspar IR_{50} signal. Analytical details and measurement protocols are given in Table S4.

Sample	Coordinates (WGS84, °N/°E, and elevation, m a.s.l.)	Radionuclide concentration			Total dose rate (Gy ka^{-1})[a]	Total number of aliquots/ grains	CAM[b] uncorrected D_e (Gy)	OD[a] (%)	FMM[c] uncorrected D_e (Gy)	g_{2days} (%/decade)	CAM* or FMM fading-corrected D_e[d] (Gy)	Age (ka)
		U (ppm)	Th (ppm)	K (%)								
VEosl_01	45.7425/7.6141/464	1.01 ± 0.11	3.92 ± 0.07	0.61 ± 0.01	2.0 ± 0.2	43	56.0 ± 11.3	96.7	27.2 ± 2.7	1.7 ± 0.8	31.9 ± 4.3	16.0 ± 2.7
VEosl_02	45.7433/7.6134/479	0.94 ± 0.26	4.14 ± 0.15	0.64 ± 0.01	2.0 ± 0.1	109	41.7 ± 2.7	63.3	26.0 ± 1.6	2.8 ± 0.8	34.6 ± 4.1	17.3 ± 2.7
PLAosl_01	45.7407/7.4300/571	1.54 ± 0.23	8.59 ± 0.43	1.14 ± 0.06	2.9 ± 0.2	159	114.3 ± 17.9	86.6	46.0 ± 3.9	3.2 ± 0.6	64.4 ± 7.4	21.5 ± 2.6
PLAosl_02	45.7409/7.4303/580	2.75 ± 0.16	10.26 ± 0.29	1.53 ± 0.02	3.7 ± 0.2	24	32.6 ± 0.7	9.7	/	3.7 ± 0.4	48.1 ± 2.5*	13.1 ± 1.1
PLAosl_03	45.7409/7.4307/584	1.72 ± 0.13	8.39 ± 0.31	1.04 ± 0.01	2.9 ± 0.2	153	155.6 ± 10.8	85.5	46.1 ± 4.6	3.1 ± 0.6	63.9 ± 8.1	21.7 ± 2.9
STPosl_01	45.7042/7.2325/640	3.41 ± 0.23	10.05 ± 0.13	1.27 ± 0.02	3.6 ± 0.2	156	36.7 ± 1.3	42.3	28.1 ± 2.9	2.8 ± 0.6	37.3 ± 4.7	10.2 ± 1.4
STPosl_02	45.7042/7.2325/640	2.92 ± 0.18	9.89 ± 0.21	1.57 ± 0.02	3.8 ± 0.2	118	37.9 ± 1.8	47.8	31.6 ± 1.4	3.1 ± 0.5	43.5 ± 3.2	11.5 ± 1.0

Samples were collected at 0.3–2.5 m depth below the surface. Coarse-grain fraction of 200–250 μm was isolated for samples VEosl_01, 02, and PLAosl_01, 03, 100–200 μm for PLAosl_02, 150–200 μm for STPosl_01, 02.
[a] Dose rate calculations were performed with DRAC (Durcan et al., 2015), assuming water content of 10 ± 5%, an internal K-content of 12.5 ± 0.5% (Huntley and Baril, 1997) and an alpha efficiency value of 0.15 ± 0.05 (Balescu and Lamothe, 1994).
[b] CAM = Central Age Model, OD = overdispersion of D_e distribution (Galbraith et al., 1999).
[c] FMM = Finite Mixture Model (Galbraith and Green, 1990). It was applied for D_e distributions with OD > 30%. A sigma-b (σ_b) value of 0.3 was used. Results obtained with 2 (STPosl_02), 3 (VEosl_02, STPosl_01) and 4 (VEosl_01, PLAosl_01, 03) multiple components were selected. No FMM was run for PLAosl_02, due to the low OD in the D_e distribution.
[d] For all the samples except PLAosl_02, fading-corrected FMM D_es are reported. For PLAosl_02, the fading-corrected CAM D_e is shown.

paleoglacial stage by interpolating the reconstructed 2D ice surfaces along the DB valley and the main tributaries in ArcGIS using the *Topo to Raster* tool (Pellitero et al., 2016). In addition, we included in the interpolation the present-day glaciers as ice-surface constraints (GlaRiskAlp Project, http://www.glariskalp.eu), based on the assumption of continuous ice coverage at high elevations since the LGM.

Lastly, equilibrium-line altitudes (ELAs) were estimated for the different reconstructed 3D ice extents. Paleo-ELAs have often been used as paleoclimatic proxy, as ELA (corresponding to the null mass-balance elevation) is primarily controlled by winter precipitation (governing ice accumulation) and summer air temperature (governing ice ablation) (e.g. Benn and Lehmkuhl, 2000; Pellitero et al., 2015; Protin et al., 2019; Baroni et al., 2021). In line with previous studies, we used three different methods to estimate paleo-ELAs (Benn and Lehmkuhl, 2000): the Toe-to-Headwall Altitude Ratio (THAR), the Accumulation Area Ratio (AAR), and the Area-Altitude Balance Ratio (AABR). For all three approaches, we adopted typical ratio values representative for alpine glaciers. For the THAR calculation, we assumed that the ELA lies at 40% of the

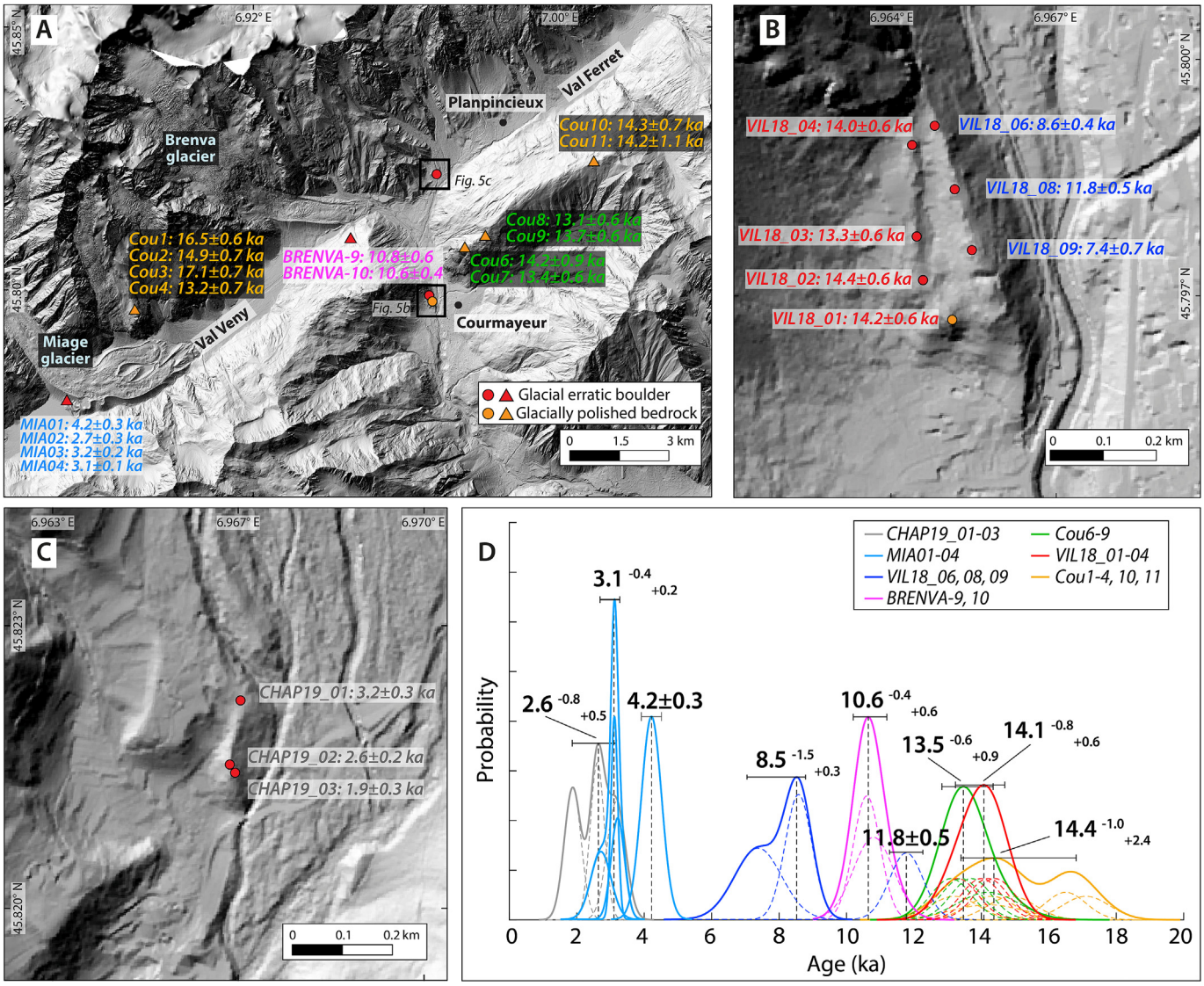

Fig. 5. Compilation of ^{10}Be surface-exposure ages in the upstream DB catchment (modified DEM from Regione Autonoma Valle d'Aosta), from this study (circles) and literature (triangles). **A)** Sample locations and re-calculated ^{10}Be surface-exposure ages of erratic boulders and polished bedrocks from literature studies. Font colour differentiates landforms/deposits. In orange and green, respectively, high- (around 2400 m a.s.l.) and low- (around 2000 m a.s.l.) altitude polished bedrocks from Wirsig et al. (2016a). In pink, erratics on till deposits at the entrance of Val Veny (Deline et al., 2015). In light blue, erratics from the Miage morainic amphitheatre (Le Roy, 2012). Black boxes highlight the two morainic complexes of Courmayeur and Chapy from the present study (panels B and C, respectively). **B)** Sample locations and ^{10}Be surface-exposure ages of the polished bedrock knob (VIL18_01) and the erratic boulders from the external (red) and internal (blue) morainic ridges of Courmayeur. **C)** Sample locations and ^{10}Be surface-exposure ages of the three erratic boulders sampled on the Chapy morainic ridge. **D)** Individual (dashed lines) and summed (continuous lines) KDE of ^{10}Be surface-exposure ages from the upstream DB catchment. Same colour code as in panels A, B and C. The modes and uncertainties of the summed KDE are reported. Sample VIL18_08 was excluded from the summed KDE of the Courmayeur internal moraine, and two separated KDEs have been calculated for Miage erratics (see text for details). (For interpretation of the references to colour in this figure legend, the reader is referred to the Web version of this article.)

altitudinal range between the lowest and highest altitude of the paleoglacier (Benn and Lehmkuhl, 2000). AAR and AABR calculations were computed using the GIS toolbox from Pellitero et al. (2015) and the reconstructed 3D ice surface as input. For the AAR approach, a value of 0.67 was assumed for the ratio of the accumulation area to the paleoglacier total area (Pellitero et al., 2015). For the AABR method, we used a balance ratio (i.e. ratio between the accumulation and ablation gradients; Osmaston, 2005) of 1.59 (average value for the European Alps; Rea, 2009).

ELA depression (ΔELA) for each reconstructed paleoglacial stage was calculated as the difference from the average LIA ELA, determined from four glaciers in the Val Ferret and Val Veny (Lex Blanche, Miage, Triolet, and Pré de Bard glaciers; Figs. 6A and S5), which are representative of the upstream DB catchment. 3D ice-surface reconstructions for LIA glaciers were obtained through the above-mentioned GIS routine, using the ice-corrected bedrock DEM (Viani et al., 2020) as glacier bed input, and fitting the ice extent to the LIA moraines (GlaRiskAlp Project, http://www.glariskalp.eu).

4. Results

4.1. Geochronology

^{10}Be surface-exposure ages obtained (Table 1) or recalculated (Table S3) in the present study are shown in Figs. 4, 5, S1 (for the

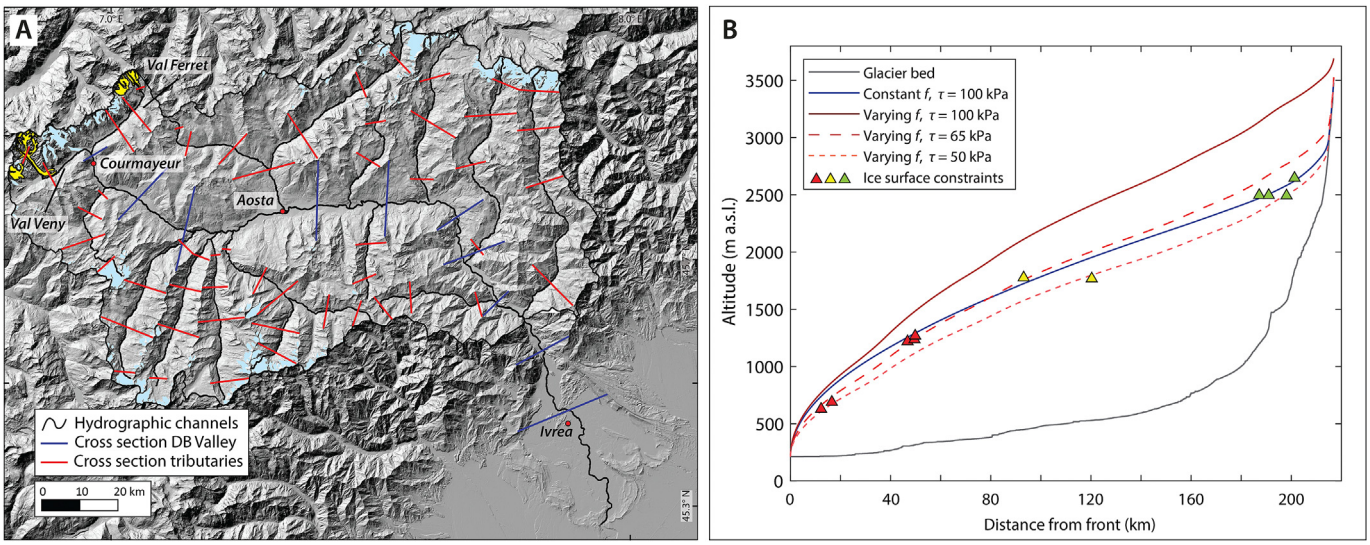

Fig. 6. Inputs and fitting of *Profiler v.2* (Benn and Hulton, 2010) for paleoglacial reconstructions. **A)** Location of modern hydrographic channels (black lines) used as glacier bed input, and of the cross sections in the DB valley (blue segments) and tributaries (red segments) for which shape factors (*f*) were calculated. Present-day glaciers (GlaRiskAlp Project, http://www.glariskalp.eu) are mapped in light blue. In yellow are the LIA extents of glaciers with ELA estimates (Fig. S5). DEM Regione Piemonte and Regione Autonoma Valle d'Aosta, downscaled to 25-m resolution. **B)** 2D ice-surface profiles for Stage 1 (ice front at the IMA) obtained for the main DB hydrographic channel (bed topography upstream of the confluence in Courmayeur was chosen following the Val Veny), for spatially-constant or -varying valley shape factor (*f*), and different shear stress (τ) values. Ice-surface geomorphic markers for Stage 1 are shown (same legend as for Fig. 1) and helped to constrain shear stress value. (For interpretation of the references to colour in this figure legend, the reader is referred to the Web version of this article.)

specific key sites) and S6 (as a summary for the entire DB catchment). Luminescence dating results are shown for each sedimentary deposit in Fig. 2, with details provided in Table 2 and Fig. 7. We focus on the D_e results obtained with the FMM on single-grain feldspar IR_{50} measurements (except for sample PLAosl_02 for which we used small aliquots and the CAM was applied), since these allowed to identify the best-bleached populations of the investigated sediments. The full details of luminescence results (IR_{50}, $pIRIR_{225}$ or $pIRIR_{150}$ on both single grains and small aliquots) are shown in the Supplementary Material (Tabs. S5, S6 and S7). We report below landform/deposit ages obtained, when possible, as the mode of summed KDE from individual ^{10}Be surface-exposure and luminescence ages (see section 3.1.1 for details). For clarity, we listed the geochronological outcomes in geographical order from piedmont to the internal DB valley (increasing distance from the IMA; Fig. 1).

For the piedmont area, four age clusters were distinguished, between the IMA and the entrance of the DB valley (newly-acquired or recalculated ^{10}Be surface-exposure ages from Gianotti et al., 2015, 2008; Fig. S1 and Table S3). From one internal IMA morainic ridge, two boulders provided ^{10}Be surface-exposure ages between 30 and 40 ka (landform age of $36.0^{-4.5}_{+4.9}$ ka; Fig. S1). For erratics on the Ivrea hills, an apparent age of $25.8^{-5.0}_{+1.6}$ ka was obtained (Fig. S1). ^{10}Be surface-exposure ages of 14.6 ± 0.6 and 19.1 ± 1.6 ka were obtained for the two polished bedrocks below the Chanton moraine (CHAN20_04 and 05, respectively; Fig. S1). CHAN20_04 provided a relatively young age that may reflect late exhumation compared to the age of abandonment of the Chanton moraine or significant erosion, and was not considered further in the discussion. Finally, a landform age of $19.0^{-1.4}_{+1.5}$ ka was recalculated for the Donnas glacially-polished bedrock at the outlet of the DB valley (Fig. S1).

In the central part of the DB catchment, luminescence burial ages of 16.0 ± 2.7 and 17.3 ± 2.7 ka were obtained within the fluviolacustrine succession of Verbion (VEosl_01 and 02, respectively, summed KDE mode of $16.7^{-2.8}_{+2.7}$ ka; Figs. 2A, 7A-B). Two luminescence ages around 22 ka (PLAols_01 and PLAols_03, summed KDE mode $21.6^{-2.7}_{+2.7}$ ka) and a younger luminescence age of 13.1 ± 1.1 ka (PLAosl_02) were calculated for La Plantaz deposits (Figs. 2C and 7C-E).

In Saint Pierre and Valgrisenche areas, two groups of ^{10}Be surface-exposure and luminescence ages could be differentiated (Fig. 4). Glacially-polished bedrock and granitic erratics from Saint Pierre hill (STP19_01–06; Fig. 4A) and micaschist boulders from Valgrisenche moraine (VGRI19_01, 02; Fig. 4B) cluster around $15.4^{-2.8}_{+0.9}$ ka (Fig. 4C). Sample STP19_02 (10.3 ± 0.5 ka) was not included in the summed KDE calculation as it appears as an outlier with a much younger age (confirmed by chronological constraints upstream in the DB valley, see Fig. 5 for details), potentially due to post-depositional shielding processes (Heyman et al., 2011). Petrological investigations suggest a Mont-Blanc origin of the granitic boulders from Saint Pierre hill, implying deposition by the main DB glacier and not by the southern tributaries, as for the micaschist boulders on the Valgrisenche moraine (Fig. 1). The other age cluster in Saint Pierre area is represented by the rockslide-derived and fluviolacustrine deposits at the outlet of Grand Eyvia tributary, showing respectively a ^{0}Be surface-exposure age of $9.3^{-0.6}_{+0.7}$ ka (POY19_01 and POY19_02; Fig. 4A and D) and a luminescence age of $11.2^{-1.8}_{+1.0}$ ka (STPosl_01 and STPosl_02; Figs. 3B and 4A and D). Petrological investigations exclude a Mont-Blanc provenance of POY19_01 and 02 gneissic boulders, and supports a more local origin.

In the DB upstream catchment, ^{10}Be surface-exposure ages were grouped in seven landform clusters (Fig. 5). Polished bedrock samples from Wirsig et al. (2016) are distinguished in two groups, based on their altitude distribution. Samples at 2400–2500 m a.s.l. (Cou1-4, 10, 11) have recalculated ages ranging from ca. 13 to 17 ka (summed KDE mode $14.4^{-1.0}_{+2.4}$ ka; Fig. 5A and D). Recalculated ages for samples at 1900–2000 m a.s.l. (Cou6-9) cluster at $13.5^{-0.6}_{+0.9}$ ka (Fig. 5A and D). Our new ^{10}Be surface-exposure ages from the external moraine of Courmayeur (VIL18_01–04, polished-bedrock knob and erratic boulders; Fig. 5B) are well clustered with a summed KDE mode at $14.1^{-0.8}_{+0.9}$ ka (Fig. 5B and D). The internal moraine provided poorly-clustered ^{10}Be surface-exposure ages,

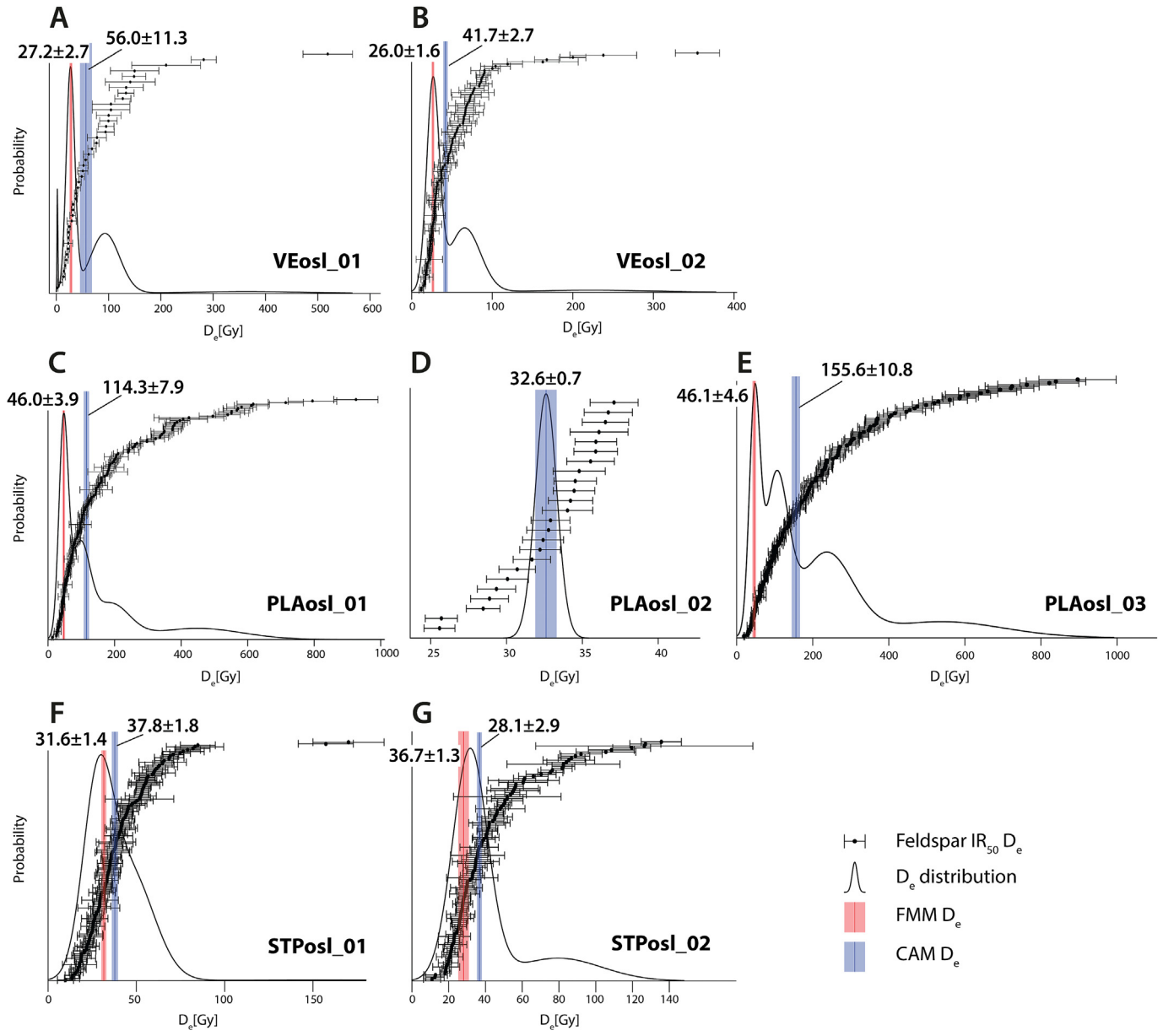

Fig. 7. Feldspar IR_{50} (single-grain for all samples except small-aliquot for PLAosl_02) D_e distributions. All the data shown are non-fading corrected. FMM summed distributions are shown with black continuous lines (all obtained with $\sigma_b = 0.3$, except CAM distribution for PLAosl_02). Red and blue vertical bars show the FMM and CAM D_e, respectively, which were subsequently fading corrected and used for burial age calculation (Table 2). (For interpretation of the references to colour in this figure legend, the reader is referred to the Web version of this article.)

potentially reflecting post-depositional moraine degradation as observed in the field. We thus calculated a summed distribution only for samples VIL18_06 and 09, providing $8.5^{-1.5}_{+0.3}$ ka (Fig. 5B and D). However, stratigraphic and geomorphic observations do not allow to discard sample VIL18_08 (11.8 ± 0.5 ka), which therefore will be also considered in the further discussion. Recalculated ^{10}Be surface-exposure ages from Val Veny (erratic boulders BRENVA-9 and 10; Deline et al., 2015) cluster at $10.6^{-0.4}_{+0.6}$ ka (Fig. 5A and D). Finally, the erratics on the Chapy moraine (CHAP19_01–03) provided ^{10}Be surface-exposure ages of 2–3.5 ka ($2.6^{-0.8}_{+0.5}$ ka; Fig. 5C and D), similar to recalculated ^{10}Be surface-exposure ages from two morainic ridges of the Miage amphitheatre (MIA01 from outer moraine at 4.2 ± 0.3 ka; MIA02-04 from inner moraine at $3.1^{-0.4}_{+0.2}$ ka; Fig. 5A and D; Le Roy, 2012).

4.2. Paleoglacial reconstructions and ELA calculations

Based on our geochronological results (section 4.1), glacial landforms/deposits identified along the DB catchment (Fig. 1) were sorted in six groups, each defining a DB ice stage from the LGM to the early Holocene (Fig. 8 and Table S1). In addition, landforms/deposits with no radiometric dating were associated to a defined ice stage based on their geomorphology and relative stratigraphy. Stage 1 (ca. 36 ka) includes landforms and deposits interpreted to

be associated to the LGM (or pre-LGM) extent of the DB glacier system: the IMA morainic ridges (Gianotti et al., 2015, 2008; Fig. S1), the Chanton lateral moraine (this study; Gianotti and Forno, 2017), the Chenez and Selva Plana till deposits (Dal Piaz et al., 2008), and the trimlines from Val Veny (Wirsig et al., 2016; Coutterand and Buoncristiani, 2006). The IMA morainic ridges provide a constraint for the DB ice front maxima, while all other landforms/deposits provide minimum estimate for the paleo-ice surface (Fig. 8A). Erratic boulders on the Ivrea hills and valley-floor polished bedrock at Donnas (Gianotti et al., 2015, 2008; Fig. S1) constrain the ice front position of Stages 2 (ca. 25 ka) and 3 (ca. 19 ka), respectively (Fig. 8A). The polished bedrocks below Chanton (CHAN20_05) were not used as ice-surface constraints, but interpreted as minimum age for ice-surface lowering (see discussion in section 5.1). Upstream in the DB catchment, Saint Pierre hill erratics and polished bedrock (Fig. 4A) and Valgrisenche lateral moraine (Fig. 4B) were correlated to the high-elevation polished bedrocks in Val Veny (Cou1-4, 10, 11, Fig. 5A; Wirsig et al., 2016) and grouped into Stage 4 (ca. 15 ka). The Saint Pierre hill deposits constrain the paleo-ice front, and the latter two landforms constrain the paleo-ice surface (Fig. 8B). The external moraine of Courmayeur (ice-front position; Fig. 5B) and the polished bedrocks above Courmayeur (ice-surface elevation; Cou6-9, Fig. 5A; Wirsig et al., 2016) were grouped into Stage 5 (ca. 14 ka; Fig. 8B). Stage 6 (ca. 10 ka) includes the internal moraine of Courmayeur (Fig. 5B) and erratic boulders at the entrance of Val Veny (Fig. 5A; Deline et al., 2015), giving constraint to the ice front and surface, respectively (Fig. 8B). The Chapy and Miage moraines (upstream of Courmayeur), with their late Holocene chronology, were not included in any DB ice stage but rather used to investigate the timing of disconnection between the Val Veny and Val Ferret glaciers.

Fig. 8 shows the six paleo-glacial profiles obtained with *Profiler v.2*. A basal shear stress value (τ) of 65 kPa was selected, in order to best fit the ice-front and -surface constraints representative of Stage 1. The obtained paleoglacial profile precisely matches the elevation of Chanton moraine and Chenez till deposit, while it overestimates the two other geomorphic constraints (Selva Plana till deposits and Val Veny trimlines 5.1). Paleoglacial profiles for Stages 2, 3, and 6 were also generated with a τ value of 65 kPa. For Stages 4 and 5, an increased τ value to 100 kPa was necessary to best-fit the observed landform/deposit constraints.

3D ice-surface reconstructions (Fig. 9) show the progressive decrease in both glacier extent and thickness throughout the six paleoglacial stages. ELA estimates from the AABR, AAR and THAR methods are shown in Figs. 9–11 and in Table 3. A trend of increasing ELA values is evident with the THAR method, especially from Stage 3 on (absolute values vary from 2090 to 2642 m a.s.l.). A general increasing trend can also be observed for the AABR ELAs (absolute values vary from 2103 to 2523 m a.s.l.). However, Stages 3 and 6 (2308 and 2473 m a.s.l., respectively) have sligthly lower values than their preceding Stages 2 and 5 (2322 and 2523 m a.s.l., respectively). No clear trend in ELA variation with ice-stage configuration can be observed for ELAs computed with the AAR method (absolute values vary from 2203 to 2428 m a.s.l.). For the LIA, average ELA values of 2888 ± 99, 2851 ± 93, and 2725 ± 139 m a.s.l. were obtained with the AABR, AAR, and THAR methods respectively (Fig. S5), leading to the ΔELA values summarised in Table 3.

5. Discussion

5.1. Post-LGM deglaciation history

By combining geomorphic and geochronological constraints with 2D ice-surface reconstructions, we identified a sequence of six (pre-)LGM to early Holocene ice stages for the DB glacial system (Figs. 8 and 9). Two assumptions were made when grouping landforms/deposits into one specific paleoglacial stage. First, for geomorphic markers without radiometric chronology (e.g. glacial till, trimline), we associated them to a given paleoglacial stage based on stratigraphic or geomorphic relationship(s). Second, we distinguished different ice dynamics for each paleoglacial stage based on the hypothesis that morainic ridges (e.g. IMA, Chanton,

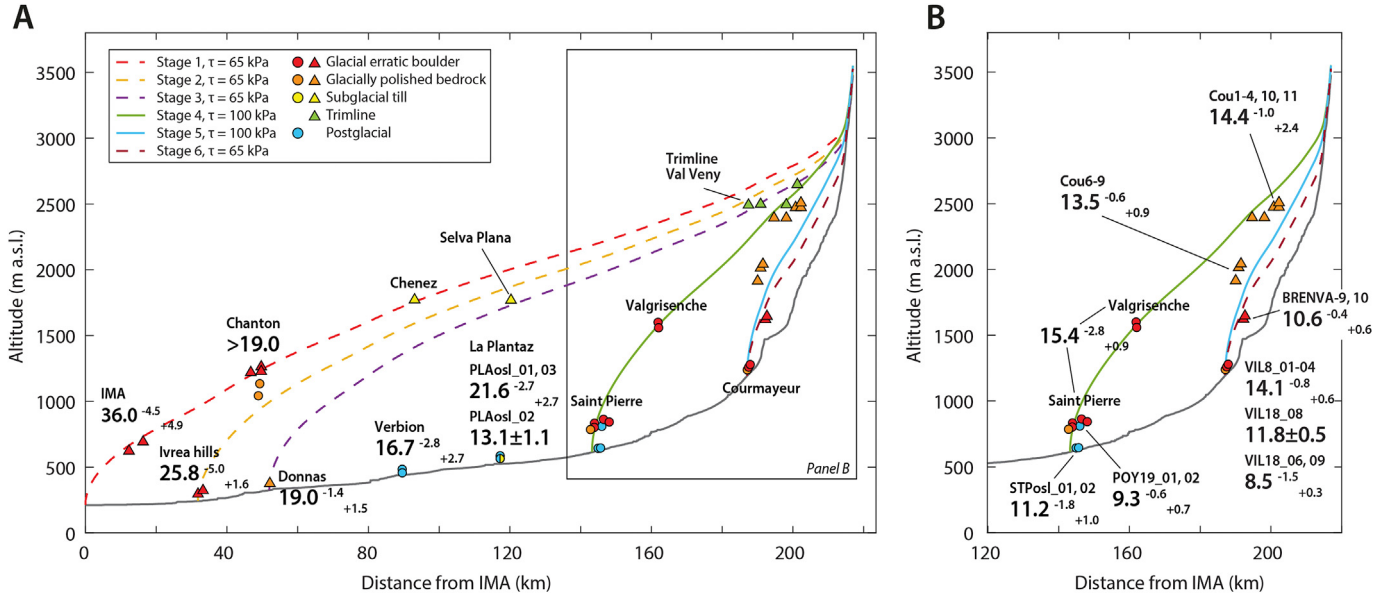

Fig. 8. 2D ice-surface profiles obtained with *Profiler v.2* (Benn and Hulton, 2010) for the six identified ice stages in the main DB hydrographic channel (bed topography upstream of the confluence in Courmayeur was chosen following the Val Veny), using different glacier basal shear stress (τ) values. Ice front and surface geomorphic constraints are shown (same legend as for Fig. 1), with their geochronological results, if available. Chronology and paleoglacial reconstruction for Stages 1–3 **(A)** and Stages 4–6 **(B)**. Holocene landforms (Chapy moraine and Miage morainic amphitheatre) are not represented, since they were not considered in the paleoglacial reconstructions.

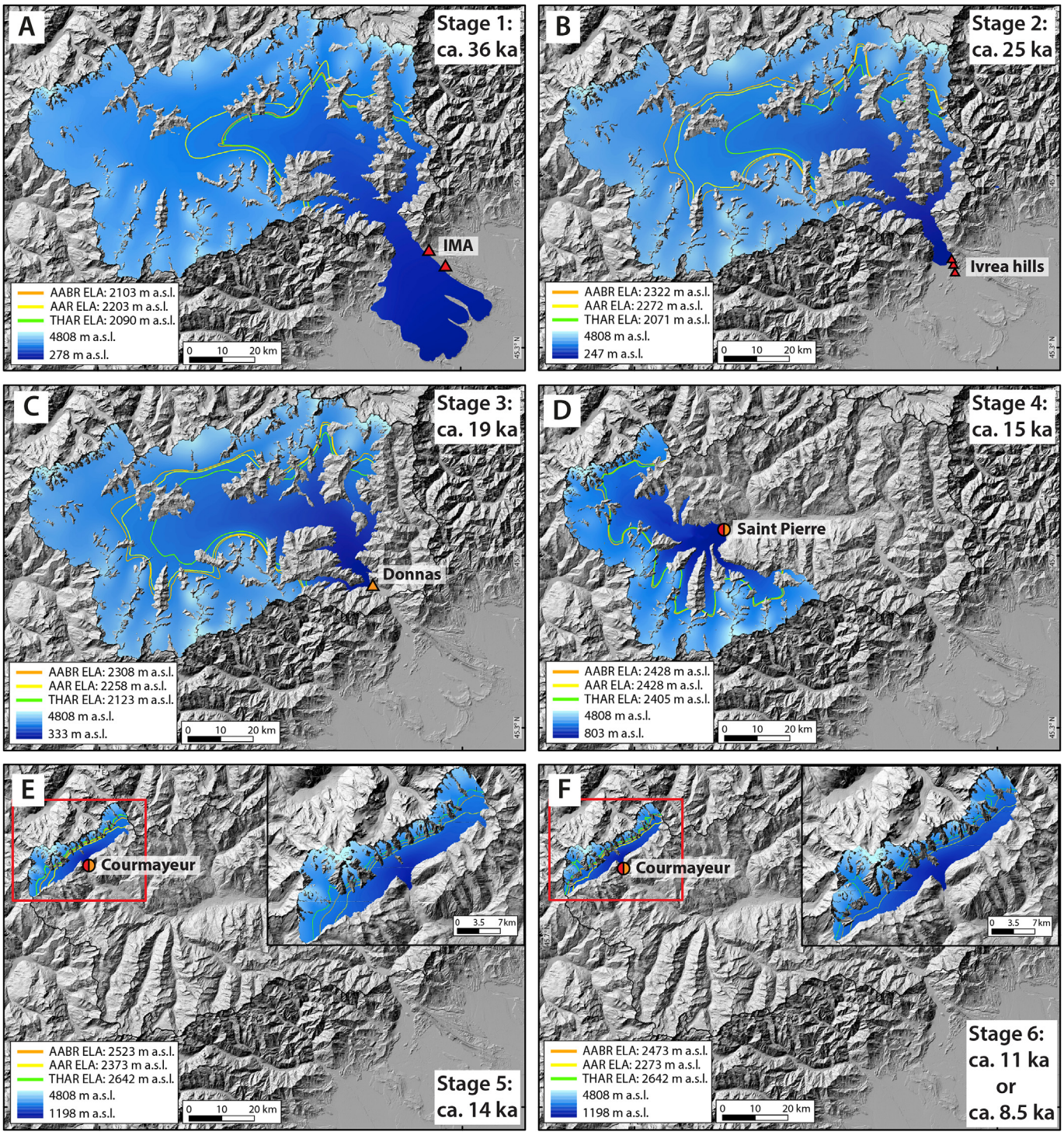

Fig. 9. 3D ice-surface reconstructions and ELA estimates of the six (pre-)LGM-Lateglacial ice stages of the DB glacier system (raster files available in the Zenodo online data repository; https://doi.org/10.5281/zenodo.5704342). Ice configurations were obtained through interpolation of 2D ice surface profiles from the DB valley (Fig. 8) and its main tributaries. Landforms/deposits used as ice-front constraints are represented (same legend as in Fig. 1). Tributary glaciers were not reconstructed after disconnecting from the main DB glacier. Reported ELAs were calculated with the ABBR, AAR, and THAR methods. Insets in panels E and F show enlargements of Stages 5 and 6 (located by red rectangle in each panel). (For interpretation of the references to colour in this figure legend, the reader is referred to the Web version of this article.)

Courmayeur; Fig. 1, S1 and 5) indicate a standing/re-advancing glacier, while erratic block fields (e.g. Ivrea hills, Saint Pierre; Fig. 1, S1 and 4) and polished bedrocks (e.g. Donnas, Saint Pierre, Courmayeur; Figs. 1, S1, 4 and 5) evidence ongoing ice retreat/thinning. In this latter case, steady-state conditions (i.e. perfect plastic ice rheology) assumed for 2D ice-surface reconstructions are not completely fulfilled, leading to potential ice-surface overestimation. However, we tried to compensate this effect by varying the basal shear stress between different paleoglacial stages (see section 4.2 for details).

Our six reconstructed paleoglacial stages along the DB valley are consistent with previously-reported post-LGM glacier history from

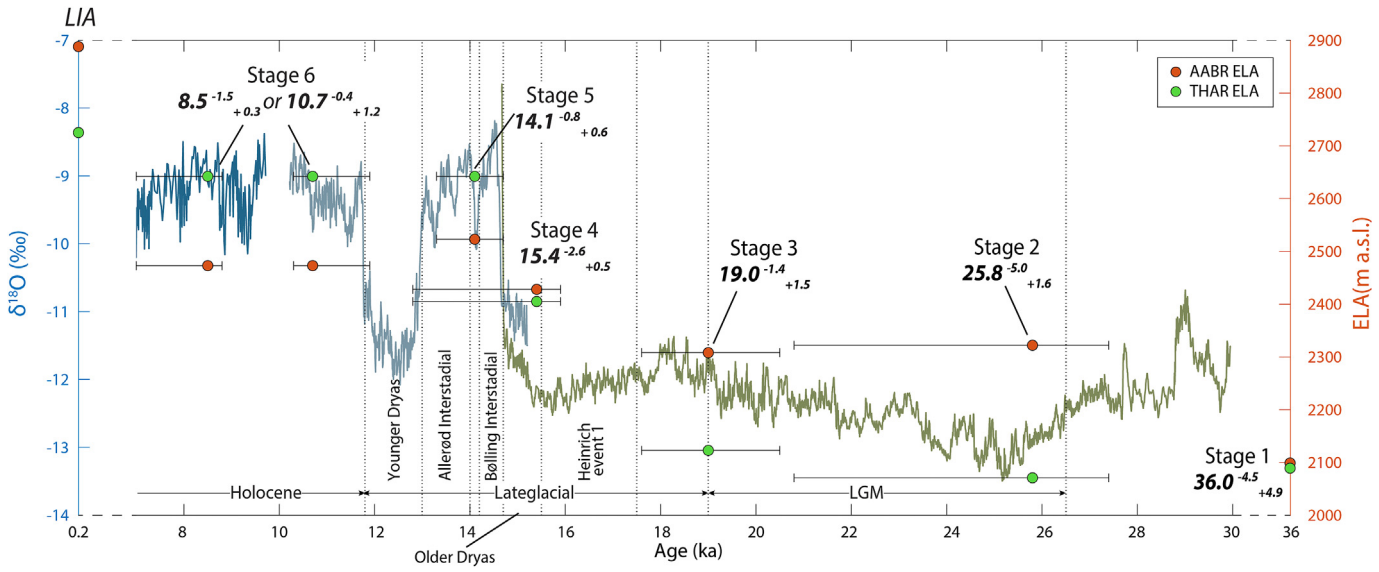

Fig. 10. Dora Baltea LGM to early Holocene paleoglacial stages in comparison with Alpine speleothems $\delta^{18}O$ climatic records. Chronology and ELA estimates of the different ice stages are based on the landforms/deposits dating constraints and paleoglacial reconstructions (Figs. 8 and 9). For stage 6, two possible chronology estimates are reported as discussed in section 5.1. ELA estimates (circles, right y-axis) are reported with the AABR and THAR method (orange and green circles respectively; Table 3). $\delta^{18}O$ record (colored lines, left y-axis) are compiled from Luetscher et al. (2015; 30.0 to 14.7 ka; green line), Li et al. (2021; 15.2 to 10.2 ka; grey line), and Regattieri et al. (2019; 9.7 to 7 ka; blue line). Black dotted lines define the temporal limits of the main Lateglacial climatic events (Stanford et al., 2011; Heiri et al., 2014b; Li et al., 2021). (For interpretation of the references to colour in this figure legend, the reader is referred to the Web version of this article.)

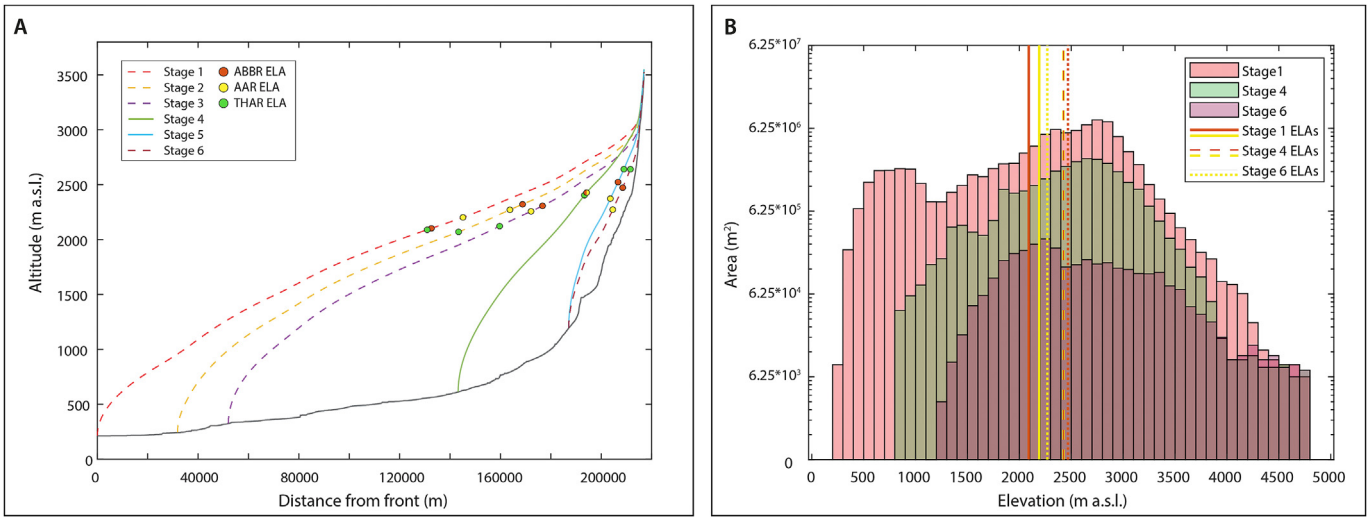

Fig. 11. ELA fluctuations and glacier hypsometry changes between different ice stages of the DB glacier system. **A)** 2D ice-surface profiles and calculated AABR, AAR and THAR ELA values, for the six stages (Fig. 9). **B)** Ice-surface hypsometry together with AABR (orange lines) and AAR (yellow lines) ELA values of Stages 1, 4, and 6. (For interpretation of the references to colour in this figure legend, the reader is referred to the Web version of this article.)

other Alpine regions, as discussed below. Furthermore, when comparing our deglaciation history with speleothems climatic records (Luetscher et al., 2015; Regattieri et al., 2019; Li et al., 2021), a connection appears between DB glacier oscillations and post-LGM Alpine climatic variability (Fig. 10).

Stage 1 (Fig. 9A) represents a possible maximum-extent of the DB glacier during the Last Glacial period, slightly pre-dating the global LGM. From pedostratigraphic investigation (Gianotti et al., 2008, 2015), the most external ridges of the IMA were already built during the penultimate glaciation (MIS 6). However, the recalculated ^{10}Be surface-exposure ages of ca. 36 ka (Fig. S1) from more internal IMA ridges alternatively suggest a possible ice re-advance during MIS 3. The IMA might thus result from multiple ice-advance episodes throughout the Late Pleistocene, with latest ice-maxima reached during the MIS 3, similar to other pre-LGM maximum ice extents reported in the southwestern Alps (Ivy-Ochs et al., 2018; Gribenski et al., 2021). Stage 2 (ca. 25 ka; Fig. 9B), defined by the ice front at the Ivrea hills (Fig. S1), coincides with the global LGM and represents an intermediary ice configuration during early retreat (Gianotti et al., 2008, 2015). Stage 3 (ca. 19 ka; Fig. 9C), with the ice front located in Donnas (Fig. S1), represents the post-LGM DB glacier which already abandoned the IMA and retreated within the mountain front, while other glacial systems in the Southern and Central Alps were still occupying the Alpine piedmonts at that time (Ravazzi et al., 2014; Ivy-Ochs et al., 2018; Braakhekke et al., 2020; Kamleitner et al., 2022). Moreover,

Table 3
Paleo-ELA and ΔELA estimates from present and literature studies. For each ice stage identified in the present study, ELA and ΔELA computed with the AABR, AAR and THAR methods are reported. ΔELAs were calculated as difference between the average LIA ELA values of Lex Blanche, Miage, Triolet, and Pré de Bard glaciers (last row of this table, Fig. S5) and the absolute ELA estimate of each ice stage reconstruction (Fig. 9). Ice front positions are indicated as distance from the IMA (Fig. 1). For each ice stage except Stage 2, a compilation of ELA and ΔELA values from the literature is reported for comparison and discussion (only ELA or ΔELA values are indicated when the original reference does not report both values).

Ice stage	Potential Alpine ice stage	Ice front position (km) and elevation (m a.s.l.)	AABR ELA (m a.s.l.) and ΔELA (m)	AAR ELA (m a.s.l.) and ΔELA (m)	THAR ELA (m a.s.l.) and ΔELA (m)	ELA (m a.s.l.) or ΔELA (m) from the literature
Stage 1	LGM or pre-LGM	0/212	2103/ −785	2203/ −648	2090/−635	- Alps ΔELA compilation = −1000 to −1500 m (AAR method; Ivy-Ochs, 2015) - Maritime Alps ELA = 1845 or 1700 m a.s.l. (ΔELA −996 or −1100 m; AABR and AAR methods, respectively; Federici et al., 2016) - DB Valley tributary ELA = 1535 m a.s.l. (AAR; Forno et al., 2010) - Susa Valley (western Italian Alps) ELA = 1600 m a.s.l. (Ivy-Ochs et al., 2018) - Toce Valley (central Italian Alps) ELA = 1500 m a.s.l. (Braakhekke et al., 2020) - Durance Valley (southern French Alps) ELA = 1800 m a.s.l. (THAR method; Jorda et al., 2000) - Clarée Valley (Southern French Alps) ELA = 2100−2200 m a.s.l. (THAR method; Cossart et al., 2012)
Stage 2	Late-LGM	32/242	2322/ −566	2272/ −579	2071/−654	
Stage 3	Early Lateglacial	52/325	2308/ −580	2258/ −593	2123/-602	- Maritime Alps ELA = 1873 or 1733 m a.s.l. (ΔELA −968 or −1077 m; AABR and AAR methods, respectively; Federici et al., 2016) - Arve glacier (French Western Alps) ΔELA = −830 m (THAR method; Coutterand and Nicoud, 2005)
Stage 4	Gschnitz stadial	143/613	2428/ −460	2428/ −423	2405/−320	- Eastern Alps ΔELA = −600 to −700 m (AAR method; Ivy-Ochs et al., 2006) - Maritime Alps ELA = 1964 or 1809 m a.s.l. (ΔELA −877 or −1001 m; AABR and AAR methods, respectively; Federici et al., 2016)
Stage 5	Daun stadial	187/1195	2523/ −365	2373/ −478	2642/−83	- Alps ΔELA compilation = −400 to −500 m (AAR method; Ivy-Ochs, 2015) - Maritime Alps ELA = 2016 or 1956 m a.s.l. m a.s.l. (ΔELA −825 or −854 m; AABR and AAR methods, respectively; Federici et al., 2016)
Stage 6	Egesen or early Holocene stadial	187/1195	2473/ −415	2273/ −578	2642/−83	- Alps Egesen ELA compilation = 1812−3270 m a.s.l. (AAR method; Baroni et al., 2021 and references therein) - Egesen ELA within or close to the DB catchment (Fig. 1): - Gran Paradiso group: 2160 ± 25 to 3300 ± 20 (ΔELA 262 m) or 2180 ± 20 to 3270 ± 15 (ΔELA 280 m) m a.s.l. (AABR and AAR method; Baroni et al., 2021 and references therein) - Mont Blanc group: 2523 (ΔELA 215) or 2648 (ΔELA 105) or 2442 (ΔELA 311) m a.s.l. (AABR and AAR method and ice model; Protin et al., 2019) - Monte Rosa group: 2750 m a.s.l. (AAR method; Gross, 1977) - Maritime Alps Egesen ELA: 2217/2368 or 2207/2305 m a.s.l. (ΔELA -624/-473 or −603/-505 m; AABR and AAR methods, respectively; Federici et al., 2016) - Maritime Alps early Holocene ELA: 2411/2640 or 2358/2617 m a.s.l. (ΔELA -420/-201 or −452/-193 m; AABR and AAR methods, respectively; Federici et al., 2016)
	LIA		2888 ± 99	2851 ± 93	2725 ± 139	- Alps LIA ELA compilation = 1973−3310 m a.s.l. (AAR method; Baroni et al., 2021 and references therein) - LIA ELA within or close to the DB catchment (Fig. 1): - Entire DB catchment: 2845 ± 165 m a.s.l. (AAR method; Vanuzzo, 2001) - Gran Paradiso group: 2590 ± 10 to 3300 ± 10 or 2590 ± 10 to 3310 ± 5 m a.s.l. (AABR and AAR method; Baroni et al., 2021 and references therein) - Mont Blanc group: 2738 or 2753 or 2753 m a.s.l. (AABR and AAR method and ice model; Protin et al., 2019) and 2702 ± 117 m a.s.l. (AAR method; Vanuzzo, 2001) - Monte Rosa group: 2903 ± 170 m a.s.l. (AAR method; Vanuzzo, 2001) - Maritime Alps ELA = 2841 or 2810 m a.s.l. (AABR and AAR methods, respectively; Federici et al., 2016)

polished bedrock below Chanton moraine provide a similar ^{10}Be age as Donnas (ca. 19 ka), suggesting that ice retreat/thinning between Stages 2 and 3 occurred rapidly during early Lateglacial (i.e. ice thinning of around 800 m in the downstream DB valley; Figs. 8 and 9).

No paleoglacial reconstruction was performed between Stages 3 and 4 (Fig. 9C and D), since neither ice-front geomorphic nor stratigraphic marker could be clearly identified and dated along this ~90-km long section of the DB valley. The absence of paleoglacial record is probably a consequence of the rapid ice retreat occurring during the early Lateglacial (Ivy-Ochs, 2015) along the overdeepened DB valley (Nicoud et al., 1999). However, both Verbion and La Plantaz sedimentary deposits provide relative minimum-age constraints on the DB glacier retreat (Fig. 1). In La Plantaz, fluvioglacial gravel and sandy strata laying on top of lodgment till were deposited at the end of the LGM (ca. 21 ka; Fig. 2C), probably at the margin of a decaying DB glacier (Stage 3; no ice-thickness constraint in La Plantaz). Similar ice-margin contact deposits (i.e. kame terrace) synchronous to early ice decay were described along the DB valley flanks (Giardino, 2005; Gianotti et al., 2008) and in the Eastern Alps (Reitner, 2007). The depositional age of Verbion fluviolacustrine succession indicates that ice withdrawal occurred before ca. 17 ka ago at this site (Fig. 2A; further discussion about Verbion paraglacial slope dynamics in section 5.3). Finally, we propose a tentative interpretation for La Plantaz fine sediments (PLAosl_02, 13.1 ± 1.1 ka; Fig. 2C) as aeolian deposits remobilized

from proglacial outwash and deposited on top of the kame terrace succesion. Such hypothesis would further support ice retreat well upstream from La Plantaz already occurring before ca. 13 ka.

Stage 4 represents the DB ice front located in Saint Pierre, ca. 15 ka ago (Fig. 9D or S7). This ice-extent configuration could correspond to the Alpine Gschnitz stadial (ca. 16 ka; Ivy-Ochs et al., 2006), a Lateglacial stage of glacier stillstand/re-advance potentially associated to the Heinrich 1 cooling event (Stanford et al., 2011, Fig. 10). At this time, the DB glacier was potentially still connected to the Gran Paradiso southern tributaries (Fig. 9D), as suggested by the similar chronology of the erratic boulders on the Saint Pierre hill and Valgrisenche moraine (Fig. 4C). Alternatively, the Gran Paradiso and DB glaciers may have been already disconnected at the Gschnitz stadial (Fig. S7), but additional age constraints from the outlet of the southern tributaries would be needed to confirm this hypothesis. Whereas the lateral moraine in Valgrisenche gives a precise ice-surface constraint for Stage 4 configuration, the erratic boulders on Saint Pierre hill rather likely indicate the onset of DB glacier retreat after the Gschnitz stadial. Likewise, the high-elevation polished bedrocks upstream of Courmayeur (Fig. 5A) most probably highlight post-Gschnitz ice thinning, in agreement with exposed polished bedrocks in the Mont Blanc massif (Lehmann et al., 2020). Several observations indicate that Saint Pierre site became ice free by at least ~12–14 ka ago: DB glacier in Courmayeur for Stages 5–6, Gran Paradiso glaciers in their internal catchments (Baroni et al., 2021), and active slope processes shortly following on site (further discussion in section 5.3).

In the Courmayeur area (most internal sector of the DB catchment, Mont Blanc massif), Stages 5 and 6 (Fig. 9E and F) were reconstructed with similar frontal positions (external and internal lateral moraines, respectively; Fig. 5B) but different ice thicknesses, constrained respectively by polished bedrocks and upstream erratics in Val Veny (Figs. 5A and 8). Despite the similar ice-extent reconstructions, our chronological data indicate at least two different periods of ice stillstands/re-advances, following the significant ice retreat from Saint Pierre (Stage 4). We propose that the DB glacier retreated from Stage 4 during the early Bølling-Allerød interstadial (Fig. 10; Heiri et al., 2014b). Potentially, Stage 5 (ca. 14 ka) could record an ice stillstand/re-advance related to a short cooling interval within the Bølling-Allerød interstadial (Older Dryas stadial or Aegelsee Oscillation, Fig. 11; Lotter et al., 1992; Samartin et al., 2012; Li et al., 2021). Within the Alpine Lateglacial chronology, Stage 5 could thus correspond to the Daun stadial (Ivy-Ochs, 2015), previously suggested as the “Courmayeur advance” by Porter and Orombelli (1982) with very similar reconstruction of paleo-ice extent (Fig. 9E). We suppose that the low-elevation polished bedrocks above Courmayeur (Cou6-9 from Wirsig et al., 2016a, Fig. 5A) were ice covered during Stage 4, and exposed during the Bølling ice retreat/thinning, with no subsequent covering during the Daun stillstand/re-advance (i.e. limited ice thickening during Stage 5; Fig. 8B). The age overlap between Cou6-9 polished bedrocks and Courmayeur external moraine boulders can possibly reflect late surface exhumation or sediment cover for Cou6-9 samples (as also proposed by Wirsig et al., 2016a).

The interpretation of Stage 6 (Fig. 9F) is less straightforward, since our ^{10}Be surface-exposure ages for the Courmayeur internal moraine are dispersed (two clusters at ca. 12 and 8.5 ka; Fig. 5). When considering VIL18_08 moraine boulder and Val Veny erratics (summed KDE at $10.7^{-0.4}_{+1.2}$ ka), Stage 6 appears as a glacier stillstand/re-advance in response to the Younger Dryas cold phase (YD, Fig. 10; Heiri et al., 2014b). The Courmayeur internal moraine would therefore be an example of Egesen stadial (Ivy-Ochs, 2015), as documented in several Alpine localities including nearby sites in the Mont Blanc and Gran Paradiso massifs (Protin et al., 2019; Baroni et al., 2021 and references therein). The Val Veny erratics would instead indicate ice decay following the YD stillstand/re-advance. Alternatively, based on our second age cluster at ca. 8.5 ka, Stage 6 could represent an early Holocene ice re-advance (e.g. Schimmelpfennig et al., 2012; Kerschner et al., 2006; Nicolussi and Schlüchter, 2012). However, distinguishing between these events remains challenging, considering the resolution and uncertainty of ^{10}Be surface-exposure dating and potential late exhumation for VIL18_06 and 09 moraine boulders. Thus, based on stratigraphy and geomorphology, none of these two interpretations can be discarded.

Finally, we propose that Val Ferret and Val Veny glaciers were still connected during both Stages 5 and 6. Porter and Orombelli (1982) supposed that during the Egesen re-advance (referred to as the “Planpincieux advance”) the Val Veny and Val Ferret glaciers were disconnected, with the Val Ferret glacier building its terminal moraine at Planpincieux (~1.5 km upstream and 200 m higher than the Chapy moraine; Fig. 5A), and the Brenva glacier front (Fig. 5A) reaching Courmayeur. Our Stage 6 ice front fits with this last proposition, but in the absence of dating of the terminal moraine at Planpincieux, the hypothesis of Val Ferret and Val Veny glaciers still connected during Stage 6 cannot be discarded. The only age constraint obtained in Val Ferret is the late Holocene (~3 ka) age for the Chapy moraine (Fig. 5C) which could be associated to a Neoglacial re-advance of Mont Fréty and Rochefort glaciers (small hanging glaciers above Chapy), similarly recognized for the nearby Miage glacier (Le Roy, 2012) and for other Alpine sites as Göschener I Oscillation (ca. 3.0–2.3 ka; Ivy-Ochs et al., 2009; Schimmelpfennig et al., 2012, 2014). Alternatively, a late-exhumation hypothesis from an older Holocene moraine deposited by a larger Val Ferret glacier cannot be fully excluded, as suggested by the distance between the Chapy moraine and present-day local glaciers, the apparent smooth ridge morphology, and the scatter in boulder exposure ages (Fig. 5C). In this case, the disconnection between Val Ferret and Val Veny glaciers would be contemporaneous to the Chapy moraine formation which, even considering a late-exhumation, should clearly postdate the YD.

5.2. Paleoglacial reconstructions and ELA fluctuations

Our paleo-ELAs, using the THAR, AAR and AABR empirical methods, present significant variability per paleoglacial stage (up to ~370 m elevation difference) and different trends throughout the deglaciation sequence (i.e. pronounced ELA increase with the THAR, moderate increase with the AABR, and almost constant ELAs with the AAR; Figs. 9 and 11, Table 3). The observed differences are related to the principles behind the three empirical methods. THAR paleo-ELA estimates only reflect the ice-front elevation increase during ice retreat, which becomes especially pronounced from Stage 4 on, when the ice-front retreats within the steeper and upper catchment (Figs. 9 and 11A). On the other hand, the AAR and AABR paleo-ELA estimates depend on the ratio between low-altitude (ablation) and high-altitude (accumulation) glacier areas. In our reconstructions, ice retreat and thinning in the low-altitude area (ablation) is weighted by ice thinning also in the high-altitude areas (Figs. 8 and 11B), resulting in general moderate to minor changes in paleo-ELAs using AABR (2103–2523 m a.s.l.) and AAR (2203–2428 m a.s.l.) methods.

Beyond the ELA inter-method variability, the general moderate ELA sensitivity compared to the significant ice decay (~180 km of ice-front retreat; Fig. 11A) during the DB Lateglacial stages is compelling. We acknowledge that our approaches for ice-surface reconstruction present potential uncertainties which could in part explain the observed paleo-ELA trends. First, as explained in previous sections, our geomorphological approach did not allow for a distinction between ice stillstand or re-advance for the considered

paleoglacial stages; however, both stages reflect significant interruption phases within the overall post-LGM trend DB glacier withdrawal, likely in response to Lateglacial climatic events. Then, 2D ice-surface profiles were obtained assuming constant shear-stress and steady state conditions using limited geomorphic markers as constraints. 3D ice surfaces were realized through geometric interpolation (with smoothing effect sometimes overestimating ice surface at the glacier front; e.g. Stage 1, Fig. 9A) and assuming synchronous ice fluctuations between the different tributaries. Lastly, glacier size, geometry and connectivity can also influence selected AAR values (Nesje, 1992; Pellitero et al., 2015). In our study, we used a constant AAR of 0.67 (typical for alpine glacier) for all paleoglacial stages, which might be inaccurate for early stages (Stages 1–4; Fig. 9). When adopting AAR value of 0.8 (more typical for large ice caps; Pellitero et al., 2015) for Stages 1–4, AAR paleo-ELA estimates indeed decrease by 200–400 m. However, besides the methodological issues highlighted above, we relate the moderate ELA changes in the DB catchment mainly to (1) the Lateglacial paleoclimate and to (2) the large size, complex topography and connectivity of the DB glacial system.

When compared with paleoclimate speleothems $\delta^{18}O$ records used as a proxy for regional climatic evolution (Fig. 10), the trend of relatively stable ELA during the early stages of deglaciation and with a clear ELA rise (pronounced for the THAR or moderate for the AABR) from Stage 4 is consistent with the relatively limited increase in temperature at the LGM-Lateglacial transition, followed by the pronounced warming of the Bølling-Allerød interstadial (14.6–12.8 ka; Fig. 11). However, the ΔELA estimates (~700 m) during the early deglaciation stages appears significantly smaller compared to other existing estimates across the Alps (Table 3; ΔELA values between 1000 and 1500 m a.s.l.) and to estimates from inverse modelling studies conducted in the European Alps (1200–1700 m; Višnjević et al., 2020), while for Stages 5–6, our paleo-ELA estimates fit within the range of paleo-ELA and ΔELA values reported from other Alpine studies: Daun (Stage 5, AAR ΔELA = −400 to −500 m; Ivy-Ochs, 2015), and Egesen to early Holocene (Stage 6, AAR ELA = 2160–3300 m a.s.l.; Baroni et al., 2021 and references therein; Federici et al., 2016).

We therefore propose that while DB paleo-ELAs reflect first-order changes in climatic conditions, external factors exert a significant limiting control on this signal, related to the large size, complex connectivity and topographic settings of the DB glacial system in the early stages of deglaciation (Stages 1–4). The DB glacial system is highly branched (i.e. many junctions from tributary catchments; Fig. 9) and expands across several topographic domains (i.e. from high-elevation steep reliefs, to low-elevation flattish valley floor and ultimately into the piedmont area). The prominent ice-front retreat along the low-lying valley floor (Stages 1–4 Fig. 11A) is associated to a limited change of ice-front elevation. In addition, ice loss appears similar between low and high elevations (Fig. 11B), therefore implying limited ELA variations despite pronounced ice withdrawal. Stage 4 appears as a transition period, and our proposed ice reconstruction already suggests an ELA rise (Fig. 10) when considering both the main DB glacier system and Gran Paradiso tributaries (Fig. 9D). However, as explained in section 5.1, we cannot exclude the potential disconnection between the DB and Gran Paradiso glacier systems already during the Gschnitz stadial (Fig. S7), resulting in lower ELA estimates (by 100–150 m) that would then be similar to Stage 3. On the contrary, Stages 5–6 are characterized by pronounced ice-front changes in elevation along the steeper topography, with larger ice loss at low elevations (Fig. 11B), resulting in ELA increase (except when considering AAR approach). During these late deglaciation stages, the DB glacier, similar to Alpine glacial systems, has retreated in the internal massifs and evolved towards simpler mountain valley glacier leading to paleo-ELA results similar to the literature (Table 3). We compared our paleo-ELA estimates with those from the Maritime Alps (Federici et al., 2016), providing similar approach for post-LGM paleo-glacier reconstructions and paleo-ELA estimates (Table 3). Despite differences in ELA absolute values, the trends in AAR and AABR paleo-ELAs throughout the successive deglaciation stages are similar between the DB catchment and the Maritime Alps, with limited paleo-ELA fluctuations (~150 m) in the early Lateglacial (LGM to Daun), when the reconstructed Gesso Valley glacier is highly-branched and retreats along a low-lying valley floor, and significant increase in paleo-ELA (~800 m) for the simple and steep valley glacier reconstructed for the Egesen stadial and the Holocene (Federici et al., 2016). Altogether, these observations suggest that paleo-ELA estimates for large-complex glacial systems, such as the LGM-Lateglacial DB glacier, are significantly influenced by the topography, and their sensitivity as paleoclimatic proxy might therefore be limited (Nesje, 1992; Pellitero et al., 2015).

We showed and discussed above the potential contribution of multiple factors (climate, topography, ELA variability across large and complex catchments) influencing paleo-ELAs reconstructions. More geomorphic constraints on paleoglacier geometry (both on ice front and surface), as well as more sophisticated ice-flow modeling for ice reconstruction and paleo-ELA quantification (Harper and Humphrey, 2003; Blard et al., 2007; Protin et al., 2019; Mey et al., 2020; Reixach et al., 2021) are therefore required when investigating complex glacial systems. Empirical ELA approaches applied in this study have instead shown to produce good paleo-ELA estimates when applied to mountain valley glaciers with simple geometry and connectivity (e.g. Bolch and Loibl, 2017), whose ELA can therefore be considered as dominantly-controlled by paleoclimate conditions and used as paleoclimate proxies. In this latter case, paleo-precipitation could also be estimated, based on paleo-temperature proxies and on the Ohmura empirical relationship between temperature and precipitation at the ELA (Spagnolo and Ribolini, 2019; Rea et al., 2020). However, given the inferred uncertainties in paleo-ELA estimates and scarcity of paleo-temperature proxies in the study area, we considered such approach outside the scope of the present study.

5.3. Post ice-retreat slope dynamics

Slope-failure processes following deglaciation have been documented in several Alpine localities (Cossart et al., 2008; Zerathe et al., 2014; Schwartz et al., 2017; Ivy-Ochs et al., 2017; Serra et al., 2021). However, their causalities still remain debated (e.g. Bigot-Cormier et al., 2005; McColl, 2012), with slope events occurring soon after deglaciation being interpreted as paraglacial processes caused by topographic glacial conditionning and post-ice retreat debutressing (e.g. Cossart et al., 2008; Grämiger et al., 2017; Serra et al., 2021), while other slope events occurring several ka after ice withdrawal have been suggested to rather result from climate warming and permafrost degradation (Cossart et al., 2008; Schwartz et al., 2017), hydrological perturbation (Zerathe et al., 2014), or even seismic events (Grämiger et al., 2016). Luminescence and ^{10}Be dating results from fluviolacustrine deposits (Verbion and Saint Pierre) and rockslide-transported boulders (Saint Pierre) give time constraints to two major slope collapse events occurring in the DB valley. Although both investigated events postdate the DB glacier withdrawal, they clearly differ in terms of time elapsed between their occurrence and local deglaciation timing, implying potentially different triggerring mechanisms (Sanchez et al., 2010).

The fluviolacustrine succession of Verbion (Figs. 1 and 2A) was previously interpreted as deposited within a rockslide-dammed lake (Mont Avi rockslide, DB right valley side, downstream of

Verbion; Giardino, 2005a). Our luminescence ages suggest sedimentation occurring at ca. 17 ka ago, therefore soon after the early-Lateglacial DB glacier retreat from Donnas (Stage 3, ca. 19 ka) to Saint Pierre (Stage 4, ca. 15 ka). This large rockslide event can thus be interpreted as paraglacial slope collapse, potentially caused by debutressing of the steep valley sides following deglaciation (e.g. Cossart et al., 2008; McColl, 2012).

The rockslide-transported boulders and fluviolacustrine deposits of Saint Pierre (Figs. 1 and 4A) show instead an early-Holocene age (ca. 9–11 ka), and fit well with the wood-derived ^{14}C age of 9240 ± 60 years BP from a nearby debris flow deposit, downstream of the confluence between the DB river and Grand Eyvia tributary (Nicoud et al., 1999, Fig. 4A). This chronology suggests that landslides from both the left (schist-boulder deposit underneath the fluviolacustrine succession; Fig. S4A; Nicoud et al., 1999) and right (POY19_01–02, gneissic boulders) DB valley flanks would have occurred ca. 4–5 ka after ice withdrawal at this site, when the DB and Gran Paradiso glaciers had already retreated in their internal catchments. Therefore, these slope-failure events are probably not from paraglacial origin, but could have been triggered by post-YD warming and associated permafrost degradation, as also proposed for other Alpine early-Holocene gravitational events (e.g. Ivy-Ochs et al., 2017). However, other possible causes (e.g. lithological fracturing; Forno et al., 2012) cannot be excluded.

6. Conclusions

By combining existing and newly-acquired chronological constraints (^{10}Be surface-exposure and luminescence burial dating) from glacial and postglacial landforms/deposits into 2D and 3D ice-surface reconstructions, our study provided a (pre-)LGM to early-Holocene deglaciation sequence for the Dora Baltea glacial system (western Italian Alps). We quantitatively reconstructed the timing and ice-configuration of six subsequent ice retreat and stillstand/re-advance stages, consistent with post-LGM glacier fluctuations described in other Alpine sectors and temporally correlated with Alpine climate oscillations.

Paleo-ELA estimates calculated with different approaches resulted in some variability for each reconstructed paleoglacial configuration, and showed contrasting evolution patterns throughout the successive deglaciation stages, with a general moderate ELA sensitivity during the early stages of deglaciation. Besides the uncertainties arising from our ice-reconstruction approach, we propose that the inter-methods ELA variability and general ELA-sensitivity trend can relate to the progressive transition of the DB glacier system in terms of ice configuration (from large and multi-branched ice system to simple and smaller valley glaciers) and topographic settings (from open and flat low-elevation valley floor to steep and constrained upper catchments). More geomorphic constraints on ice geometry as well as more sophisticated ice-flow modeling for ice reconstruction are therefore required to obtain more precise and representative ELA estimates for such large and complex glacial systems.

Finally, we also provided chronological constraints for two major slope-collapse events, occurring in the DB valley after ice withdrawal. Potential different triggering mechanisms were proposed for the two events, based on the time difference between their occurrence and the local deglaciation.

Author contributions

ES, PGV and NG designed the study. ES, PGV, NG and PD performed field investigations and sample collection. ES performed ^{10}Be cosmogenic analysis (with JC), luminescence analysis (with NG and PGV) and paleoglacial reconstructions. ES wrote the manuscript with input from all co-authors.

Declaration of competing interest

The authors declare that they have no known competing financial interests or personal relationships that could have appeared to influence the work reported in this paper.

Acknowledgements

The authors warmly thank R. Delunel and F. Magrani for the help during fieldwork. J. Krbanjevic is thanked for support for ^{10}Be surface exposure dating sample preparation. J. Vieira Duarte and F. Piccoli are thanked for the help with sample petrological investigation. The authors warmly thank the ASTER team for the measurements performed at the ASTER AMS facility (CEREGE, Aix-en-Provence). M. Spagnolo, one anonymous reviewer and the editor G. Zanchetta are thanked for constructive reviews and suggestions which improved the quality of our manuscript. This study was supported by the Swiss National Science Foundation SNSF (Grant PP00P2_170559) and the French ANR-PIA programme (ANR-18-MPGA-0006). All data are available in tables in the main text and online supporting information.

Appendix A. Supplementary data

Supplementary data to this article can be found online at https://doi.org/10.1016/j.quascirev.2022.107446.

References

Affolter, S., Häuselmann, A., Fleitmann, D., Lawrence Edwards, R., Cheng, H., Leuenberger, M., 2019. Central Europe temperature constrained by speleothem fluid inclusion water isotopes over the past 14,000 years. Sci. Adv. 5, 1–10. https://doi.org/10.1126/sciadv.aav3809.

Anderson, B., MacKintosh, A., 2012. Controls on mass balance sensitivity of maritime glaciers in the Southern Alps, New Zealand: the role of debris cover. J. Geophys. Res. Earth Surf. 117, 1–15. https://doi.org/10.1029/2011JF002064.

André, M.F., 2002. Rates of postglacial rock weathering on glacially scoured outcrops (Abisko–Riksgränsen area, 68 N). Geogr. Ann. Phys. Geogr. 84 (3–4), 139–150.

Arnold, M., Merchel, S., Bourlès, D.L., Braucher, R., Benedetti, L., Finkel, R.C., Aumaître, G., Gottdang, A., Klein, M., 2010. The French accelerator mass spectrometry facility ASTER: improved performance and developments. Nucl. Instrum. Methods Phys. Res. Sect. B Beam Interact. Mater. Atoms 268, 1954–1959. https://doi.org/10.1016/J.NIMB.2010.02.107.

Auclair, M., Lamothe, M., Huot, S., 2003. Measurement of anomalous fading for feldspar IRSL using SAR. Radiat. Meas. 37, 487–492. https://doi.org/10.1016/S1350-4487(03)00018-0.

Badino, F., Ravazzi, C., Valle, F., Pini, R., Aceti, A., Brunetti, M., Champvillair, E., Maggi, V., Maspero, F., Perego, R., Orombelli, G., 2018. 8800 years of high-altitude vegetation and climate history at the Rutor Glacier forefield, Italian Alps. Evidence of middle Holocene timberline rise and glacier contraction. Quat. Sci. Rev. 185, 41–68. https://doi.org/10.1016/j.quascirev.2018.01.022.

Balescu, S., Lamothe, M., 1994. Comparison of TL and IRSL age estimates of feldspar coarse grains from waterlain sediments. Quat. Sci. Rev. 13, 437–444.

Baroni, C., Gennaro, S., Cristina, M., Ivy-ochs, S., Christl, M., Cerrato, R., Orombelli, G., 2021. Last Lateglacial glacier advance in the Gran Paradiso Group reveals relatively drier climatic conditions established in the Western Alps since at least the Younger Dryas. Quat. Sci. Rev. 255, 106815. https://doi.org/10.1016/j.quascirev.2021.106815.

Becker, P., Seguinot, J., Jouvet, G., Funk, M., 2016. Last Glacial Maximum precipitation pattern in the Alps inferred from glacier modelling. Geograph. Helv. 71 (3), 173–187.

Benn, D.I., Hulton, N.R.J., 2010. An Excel^{TM} spreadsheet program for reconstructing the surface profile of former mountain glaciers and ice caps. Comput. Geosci. 36, 605–610. https://doi.org/10.1016/j.cageo.2009.09.016.

Benn, D.I., Lehmkuhl, F., 2000. Mass balance and equilibrium-line altitudes of glaciers in high-mountain environments. Quat. Int. 65, 15–29. https://doi.org/10.1016/S1040-6182(99)00034-8.

Bigot-Cormier, F., Braucher, R., Bourlès, D., Guglielmi, Y., Dubar, M., Stéphan, J.F., 2005. Chronological constraints on processes leading to large active landslides. Earth Planet Sci. Lett. 235, 141–150. https://doi.org/10.1016/j.epsl.2005.03.012.

Blard, P.H., Lavé, J., Pik, R., Wagnon, P., Bourlès, D., 2007. Persistence of full glacial conditions in the central Pacific until 15,000 years ago. Nature 449, 591–594. https://doi.org/10.1038/nature06142.

Bolch, T., Loibl, D., 2017. GIS for glaciers and glacial landforms. In: Huang, Bo. Comprehensive Geographic Information Systems. Elsevier, Amsterdam, pp. 112–139.

Boxleitner, M., Ivy-Ochs, S., Egli, M., Brandova, D., Christl, M., Maisch, M., 2019. Lateglacial and early Holocene glacier stages - new dating evidence from the meiental in central Switzerland. Geomorphology 340, 15–31. https://doi.org/10.1016/j.geomorph.2019.04.004.

Böhlert, R., Egli, M., Maisch, M., Brandová, D., Ivy-Ochs, S., Kubik, P.W., Haeberli, W., 2011. Application of a combination of dating techniques to reconstruct the Lateglacial and early Holocene landscape history of the Albula region (eastern Switzerland). Geomorphology 127 (1–2), 1–13.

Braakhekke, J., Ivy-Ochs, S., Monegato, G., Gianotti, F., Martin, S., Casale, S., Christl, M., 2020. Timing and flow pattern of the orta glacier (European Alps) during the last glacial maximum. Boreas bor 12427. https://doi.org/10.1111/bor.12427.

Braucher, R., Guillou, V., Bourlès, D.L., Arnold, M., Aumaître, G., Keddadouche, K., Nottoli, E., 2015. Preparation of ASTER in-house $^{10}Be/^{9}Be$ standard solutions. Nucl. Instrum. Methods Phys. Res. Sect. B Beam Interact. Mater. Atoms 361, 335–340. https://doi.org/10.1016/j.nimb.2015.06.012.

Brown, E.T., Edmond, J.M., Raisbeck, G.M., Yiou, F., Kurz, M.D., Brook, E.J., 1991. Examination of surface exposure ages of Antarctic moraines using in situ produced 10Be and 26Al. Geochem. Cosmochim. Acta 55, 2269–2283. https://doi.org/10.1016/0016-7037(91)90103-C.

Buylaert, J.P., Murray, A.S., Thomsen, K.J., Jain, M., 2009. Testing the potential of an elevated temperature IRSL signal from K-feldspar. Radiat. Meas. 44, 560–565. https://doi.org/10.1016/j.radmeas.2009.02.007.

Carraro, F., Lanza, R., Perotto, A., Zanella, E., 1991. L'evoluzione morfologica del Biellese occidentale durante il Pliestocene inferiore e medio, in relazione all'inizio della costruzione dell'Anfiteatro Morenico d'Ivrea. Boll. Museo Reg. Sc. Nat. Torino 9 (1), 99–117.

Chenet, M., Brunstein, D., Jomelli, V., Roussel, E., Rinterknecht, V., Mokadem, F., Biette, M., Robert, V., Léanni, L., ASTER Team, 2016. ^{10}Be cosmic-ray exposure dating of moraines and rock avalanches in the Upper Romanche valley (French Alps): evidence of two glacial advances during the Late Glacial/Holocene transition. Quat. Sci. Rev. 148, 209–221.

Clark, P.U., Dyke, A.S., Shakun, J.D., Carlson, A.E., Clark, J., Wohlfarth, B., Mitrovica, J.X., Hostetler, S.W., McCabe, A.M., 2009. The last glacial maximum. Science 325, 710–714. https://doi.org/10.1126/science.1172873.

Claude, A., Ivy-Ochs, S., Kober, F., Antognini, M., Salcher, B., Kubik, P.W., 2014. The Chironico landslide (Valle Leventina, southern Swiss Alps): age and evolution. Swiss J. Geosci. 107, 273–291. https://doi.org/10.1007/s00015-014-0170-z.

Colarossi, D., Duller, G.A.T., Roberts, H.M., Tooth, S., Lyons, R., 2015. Comparison of paired quartz OSL and feldspar post-IR IRSL dose distributions in poorly bleached fluvial sediments from South Africa. Quat. Geochronol. 30, 233–238. https://doi.org/10.1016/j.quageo.2015.02.015.

Cossart, E., Braucher, R., Fort, M., Bourlès, D.L., Carcaillet, J., 2008. Slope instability in relation to glacial debuttressing in alpine areas (Upper Durance catchment, southeastern France): evidence from field data and ^{10}Be cosmic ray exposure ages. Geomorphology 95, 3–26. https://doi.org/10.1016/j.geomorph.2006.12.022.

Cossart, E., Fort, M., Bourlès, D., Braucher, R., Perrier, R., Siame, L., 2012. Deglaciation pattern during the Lateglacial/Holocene transition in the southern French Alps. Chronological data and geographical reconstruction from the Clarée Valley (upper Durance catchment, southeastern France). Palaeogeogr. Palaeoclimatol. Palaeoecol. 315–316, 109–123. https://doi.org/10.1016/j.palaeo.2011.11.017.

Coutterand, S., Buoncristiani, J.F., 2006. Paléogéographie du dernier maximum glaciaire du pléistocène récent de la région du massif du Mont Blanc, France. Quaternaire 17, 35–43. https://doi.org/10.4000/quaternaire.633.

Coutterand, S., Nicoud, G., 2005. Les stades de retrait du glacier de l'Arve entre le verrou de cluses et l'ombilic de chamonix au cours du tardiglaciaire (Vallée de l'Arve, Haute-Savoie). Quaternaire 16, 85–94. https://doi.org/10.4000/quaternaire.296.

Cuffey, K.M., Paterson, W.S.B., 2010. The Physics of Glaciers. Accedemic Press.

Dal Piaz, G.V., Gianotti, F., Monopoli, B., Pennacchioni, G., Tartarotti, P., Schiavo, A., 2008. Carta Geologica d'Italia - Foglio 091 (Chatillon).

Davis, P.T., Menounos, B., Osborn, G., 2009. Holocene and latest Pleistocene alpine glacier fluctuations: a global perspective. Quat. Sci. Rev. 28, 2021–2033. https://doi.org/10.1016/j.quascirev.2009.05.020.

Decaulne, A., Cossart, E., Mercier, D., Feuillet, T., Coquin, J., Jónsson, H.P., 2016. An early Holocene age for the Vatn landslide (Skagafjörður, central northern Iceland): insights into the role of postglacial landsliding on slope development. Holocene 26, 1304–1318. https://doi.org/10.1177/0959683616638432.

Deline, P., Akçar, N., Ivy-Ochs, S., Kubik, P.W., 2015. Repeated Holocene rock avalanches onto the Brenva glacier, Mont Blanc massif, Italy: a chronology. Quat. Sci. Rev. 126, 186–200. https://doi.org/10.1016/j.quascirev.2015.09.004.

Diolaiuti, G.A., Bocchiola, D., Vagliasindi, M., D'Agata, C., Smiraglia, C., 2012. The 1975-2005 glacier changes in Aosta Valley (Italy) and the relations with climate evolution. Prog. Phys. Geogr. 36, 764–785. https://doi.org/10.1177/0309133312456413.

Duller, G.A.T., 2008. Single-grain optical dating of Quaternary sediments: why aliquot size matters in luminescence datin. Boreas 37, 589–612. https://doi.org/10.1111/j.1502-3885.2008.00051.x.

Dunne, J., Elmore, D., Muzikar, P., 1999. Scaling factors for the rates of production of cosmogenic nuclides for geometric shielding and attenuation at depth on sloped surfaces. Geomorphology 27, 3–11. https://doi.org/10.1016/S0169-555X(98)00086-5.

Durcan, J.A., King, G.E., Duller, G.A.T., 2015. DRAC: dose rate and age calculator for trapped charge dating. Quat. Geochronol. 28, 54–61. https://doi.org/10.1016/j.quageo.2015.03.012.

Federici, P.R., Ribolini, A., Spagnolo, M., 2016. Glacial history of the maritime Alps from the last glacial maximum to the Little ice age. Geol. Soc. London, Spec. Publ. 433, 137–159. https://doi.org/10.1144/sp433.9.

Florineth, D., Schlüchter, C., 2000. Alpine evidence for atmospheric circulation patterns in europe during the last glacial maximum. Quaternary Research 54 (3), 295–308.

Forno, M.G., Gattiglio, M., Gianotti, F., 2012. Geological context of the becca France historical landslide (Aosta valley, NW Italy). Alp. Mediterr. Quat. 25, 125–140.

Forno, M.G., Gianotti, F., Gianluca, R., 2010. Significato paleoclimatico dei rapporti tra il glacialismo principale e quello tributario nella Bassa Valle della Dora Baltea. Il Quternario. Italian Journal of Quaternary Sciences 23 (1), 105–124.

Gaar, D., Graf, H.R., Preusser, F., 2019. New chronological constraints on the timing of Late Pleistocene glacier advances in northern Switzerland. E& G Quat. Sci. J. 68, 53–73. https://doi.org/10.5194/egqsj-68-53-2019.

Galbraith, R.F., Green, P.F., 1990. Estimating the component ages in a finite mixture. Int. J. Radiat. Appl. Instrumentation. Part 17, 197–206. https://doi.org/10.1016/1359-0189(90)90035-V.

Galbraith, R.F., Roberts, R.G., 2012. Statistical aspects of equivalent dose and error calculation and display in OSL dating: an overview and some recommendations. Quat. Geochronol. 11, 1–27. https://doi.org/10.1016/j.quageo.2012.04.020.

Galbraith, R.F., Roberts, R.G., Laslett, G.M., Yoshida, H., Olley, J.M., 1999. Optical dating of single and multiple grains of quartz from jinmium rock shelter, northern Australia: part i, experimental design and statistical models. Archaeometry 2, 339–364.

Gianotti, F., Forno, M.G., 2017. Il Quaternario della Conca di Aosta nell'ambito del modellamento glaciale del bacino della Dora Baltea. Geol. dell'Ambiente - Ital. Mag. Environ. Geol.

Gianotti, F., Forno, M.G., Ivy-Ochs, S., Kubik, P.W., 2008. New chronological and stratigraphical data on the Ivrea amphitheatre (Piedmont, NW Italy). Quat. Int. 190, 123–135. https://doi.org/10.1016/j.quaint.2008.03.001.

Gianotti, F., Forno, M.G., Ivy-Ochs, S., Monegato, G., Pini, R., Ravazzi, C., 2015. Stratigraphy of the ivrea morainic amphitheatre (NW Italy): an updated synthesis. Alp. Mediterr. Quat. 28, 29–58.

Giardino, M., 2005a. Encadré : Sédimentation et néotectonique post-glaciaires dans la moyenne Vallée d'Aoste. Collect. EDYTEM. Cah. géographie, numéro 3, 2005. Le Quaternaire des vallées alpines. Fronts glaciaires, mouvements de versant, comblements alluviaux dans les vallées de l'Arve, d'Aoste et de Suse. Livret-guide de l'excursion organisée par l'AFEQ du 2 au 4 juin 2005 114–120 https://doi.org/https://doi.org/10.3406/edyte.2005.927.

Giardino, M., 2005b. Arrêt 2 -Formes et dépôts de la glaciation pléistocène dans la moyenne Vallée d'Aoste (Carrière de la Plantaz). Collect. EDYTEM. Cah. géographie, numéro 3, 2005. Le Quaternaire des vallées alpines. Fronts glaciaires, mouvements de versant, comblements alluviaux dans les vallées de l'Arve, d'Aoste et de Suse. Livret-guide de l'excursion organisée par l'AFEQ du 2 au 4 juin 2005 97–103 https://doi.org/https://doi.org/10.3406/edyte.2005.925.

Gosse, J.C., Phillips, F.M., 2001. Terrestrial in situ cosmogenic nuclides: theory and application. Quat. Sci. Rev. 20, 1475–1560. https://doi.org/10.1016/S0277-3791(00)00171-2.

Grämiger, L.M., Moore, J.R., Gischig, V.S., Ivy-Ochs, S., Loew, S., 2017. Beyond debuttressing: mechanics of paraglacial rock slope damage during repeat glacial cycles. J. Geophys. Res. Earth Surf. 122, 1004–1036. https://doi.org/10.1002/2016JF003967.

Grämiger, L.M., Moore, J.R., Vockenhuber, C., Aaron, J., Hajdas, I., Ivy-Ochs, S., 2016. Two early Holocene rock avalanches in the bernese Alps (rinderhorn, Switzerland). Geomorphology 268, 207–221. https://doi.org/10.1016/J.GEOMORPH.2016.06.008.

Gribenski, N., Jansson, K.N., Preusser, F., Harbor, J.M., Stroeven, A.P., Trauerstein, M., Blomdin, R., Heyman, J., Caffee, M.W., Lifton, N.A., Zhang, W., 2018. Re-evaluation of MIS 3 glaciation using cosmogenic radionuclide and single grain luminescence ages, Kanas Valley, Chinese Altai. J. Quat. Sci. 33, 55–67. https://doi.org/10.1002/jqs.2998.

Gribenski, N., Valla, P.G., Preusser, F., Roattino, T., Crouzet, C., Buoncristiani, J.-F., 2021. Out-of-phase Late Pleistocene glacial maxima in the Western Alps reflect past changes in North Atlantic atmospheric circulation. Geology accepted. https://doi.org/10.1130/G48688.1.

Harper, J.T., Humphrey, N.F., 2003. High altitude Himalayan climate inferred from glacial ice flux. Geophys. Res. Lett. 30 (14), 1764. https://doi.org/10.1029/2003GL017329.

Heiri, O., Brooks, S.J., Renssen, H., Bedford, A., Hazekamp, M., Ilyashuk, B., Jeffers, E.S., Lang, B., Kirilova, E., Kuiper, S., Millet, L., Samartin, S., Toth, M., Verbruggen, F., Watson, J.E., Van Asch, N., Lammertsma, E., Amon, L., Birks, H.H., Birks, H.J.B., Mortensen, M.F., Hoek, W.Z., Magyari, E., Munõz Sobrino, C., Seppä, H., Tinner, W., Tonkov, S., Veski, S., Lotter, A.F., 2014a. Validation of climate model-inferred regional temperature change for late-glacial Europe. Nat. Commun. 5, 1–7. https://doi.org/10.1038/ncomms5914.

Heiri, O., Koinig, K.A., Spötl, C., Barrett, S., Brauer, A., Drescher-Schneider, R., Gaar, D., Ivy-Ochs, S., Kerschner, H., Luetscher, M., Moran, A., Nicolussi, K., Preusser, F., Schmidt, R., Schoeneich, P., Schwörer, C., Sprafke, T., Terhorst, B., Tinner, W.,

2014b. Palaeoclimate records 60-8 ka in the Austrian and Swiss Alps and their forelands. Quat. Sci. Rev. 106, 186–205. https://doi.org/10.1016/j.quascirev.2014.05.021.
Heyman, J., Stroeven, A.P., Harbor, J.M., Caffee, M.W., 2011. Too young or too old: evaluating cosmogenic exposure dating based on an analysis of compiled boulder exposure ages. Earth Planet Sci. Lett. 302, 71–80. https://doi.org/10.1016/j.epsl.2010.11.040.
Hofmann, F.M., Alexanderson, H., Schoeneich, P., Mertes, J.R., Leanni, L., , Aster Team, Aumaître, Georges, Bourlès, Didier L., Keddadouche, Karim, 2019. Post-Last Glacial Maximum glacier fluctuations in the southern Écrins massif (western-most Alps): insights from ^{10}Be cosmic ray exposure dating. Boreas 48 (4), 1019–1041.
Holzhauser, H., Magny, M., Zumbühl, H.J., 2005. Glacier and lake-level variations in west-central Europe over the last 3500 years. Holocene 15, 789–801. https://doi.org/10.1191/0959683605hl853ra.
Huntley, D.J., Baril, M.R., 1997. The K content of the K-feldspars being measured in optical dating or in thermoluminescence dating. Anc. TL 15, 11–13.
Huntley, D.J., Lamothe, M., 2011. Ubiquity of anomalous fading in K-feldspars and the measurement and correction for it in optical dating. Can. J. Earth Sci. 38, 1093–1106. https://doi.org/10.1139/e01-013.
Ilyashuk, E.A., Koinig, K.A., Heiri, O., Ilyashuk, B.P., Psenner, R., 2011. Holocene temperature variations at a high-altitude site in the Eastern Alps: a chironomid record from Schwarzsee ob Sölden, Austria. Quat. Sci. Rev. 30, 176–191. https://doi.org/10.1016/j.quascirev.2010.10.008.
Isotta, F.A., Frei, C., Weilguni, V., Perčec Tadić, M., Lassègues, P., Rudolf, B., Pavan, V., Cacciamani, C., Antolini, G., Ratto, S.M., Munari, M., Micheletti, S., Bonati, V., Lussana, C., Ronchi, C., Panettieri, E., Marigo, G., Vertačnik, G., 2014. The climate of daily precipitation in the Alps: development and analysis of a high-resolution grid dataset from pan-Alpine rain-gauge data. Int. J. Climatol. 34, 1657–1675. https://doi.org/10.1002/joc.3794.
Ivy-Ochs, S., 2015. Glacier variations in the European Alps at the end of the last glaciation. Cuadernos Invest. Geogr. 41, 295. https://doi.org/10.18172/cig.2750.
Ivy-Ochs, S., Kerschner, H., Kubik, P.W., Schlüchter, C., 2006. glacier response in the European Alps to Heinrich event 1 cooling: the Gschnitz stadial. J. Quat. Sci. 21, 115–130. https://doi.org/10.1002/jqs.955.
Ivy-Ochs, S., Kerschner, H., Maisch, M., Christl, M., Kubik, P.W., Schlüchter, C., 2009. Latest Pleistocene and Holocene glacier variations in the European Alps. Quat. Sci. Rev. 28, 2137–2149. https://doi.org/10.1016/j.quascirev.2009.03.009.
Ivy-Ochs, S., Kerschner, H., Schlüchter, C., 2007. Cosmogenic nuclides and the dating of Lateglacial and Early Holocene glacier variations: the Alpine perspective. Quat. Int. 164, 53–63.
Ivy-Ochs, S., Lucchesi, S., Baggio, P., Fioraso, G., Gianotti, F., Monegato, G., Graf, A.A., Akçar, N., Christl, M., Carraro, F., Forno, M.G., Schlüchter, C., 2018. New geomorphological and chronological constraints for glacial deposits in the Rivoli-Avigliana end-moraine system and the lower Susa Valley (Western Alps, NW Italy). J. Quat. Sci. 33, 550–562. https://doi.org/10.1002/jqs.3034.
Ivy-Ochs, S., Martin, S., Campedel, P., Hippe, K., Alfimov, V., Vockenhuber, C., Andreotti, E., Carugati, G., Pasqual, D., Rigo, M., Viganò, A., 2017. Geomorphology and age of the Marocche di Dro rock avalanches (Trentino, Italy). Quat. Sci. Rev. 169, 188–205. https://doi.org/10.1016/J.QUASCIREV.2017.05.014.
Jorda, M., Rosique, T., Évin, J., 2000. Données nouvelles sur l'âge du dernier maximum glaciaire dans les Alpes méridionales françaises. Comptes Rendus Acad. Sci. - Ser. IIA Earth Planet. Sci. 331, 187–193.
Kamleitner, S., Ivy-Ochs, S., Monegato, G., Gianotti, F., Akçar, N., Vockenhuber, C., Christl, M., Synal, H.A., 2022. The ticino-toce glacier system (Swiss-Italian Alps) in the framework of the alpine last glacial maximum. Quat. Sci. Rev. 279, 107400. https://doi.org/10.1016/j.quascirev.2022.107400.
Kerschner, H., Hertl, A., Gross, G., Ivy-Ochs, S., Kubik, P.W., 2006. Surface exposure dating of moraines in the Kromer valley (Silvretta Mountains, Austria) - evidence for glacial response to the 8.2 ka event in the Eastern Alps? Holocene 16, 7–15. https://doi.org/10.1196/0959683606hl902rp.
Kerschner, H., Ivy-Ochs, S., 2008. Palaeoclimate from glaciers: examples from the eastern Alps during the alpine lateglacial and early Holocene. Global Planet. Change 60, 58–71. https://doi.org/10.1016/j.gloplacha.2006.07.034.
Kirkbride, M.P., Winkler, S., 2012. Correlation of Late Quaternary moraines: impact of climate variability, glacier response, and chronological resolution. Quat. Sci. Rev. 46, 1–29. https://doi:10.1016/j.quascirev.2012.04.002.
Kohl, C., Nishiizumi, K., 1992. Chemical isolation of quartz for measurement of in-situ -produced cosmogenic nuclides. Geochem. Cosmochim. Acta 56, 3583–3587. https://doi.org/10.1016/0016-7037(92)90401-4.
Kreutzer, S., 2020. calc_FadingCorr( ): apply a fading correction according to Huntley & Lamothe (2001) for a given g-value and a given tc. Function version 0.4.2. In: Kreutzer, S., Burow, C., Dietze, M., Fuchs, M.C., Schmidt, C., Fischer, M., Friedrich, J. (Eds.), 2020. Luminescence: Comprehensive Luminescence Dating Data Analysis. R Package Version 0.9.7. https://CRAN.R-project.org/package=Luminescence.
Kreutzer, S., Burow, C., 2020. analyse_FadingMeasurement( ): analyse fading measurements and returns the fading rate per decade (g-value). Function version 0.1.11. In: Kreutzer, S., Burow, C., Dietze, M., Fuchs, M.C., Schmidt, C., Fischer, M., Friedrich, J. (Eds.), Luminescence: Comprehensive Luminescence Dating Data Analysis. R Package Version 0.9.7. https://CRAN.R-project.org/package=Luminescence, 2020.
Le Roy, M., 2012. Reconstitution des fluctuations glaciaires holocenes dansl es Alpes occidentales - Apports de la dendrochronologie et des datations par isotopes cosmogeniques produits in-situ (Doctoral dissertation, Grenoble).
Le Roy, M., Deline, P., Carcaillet, J., Schimmelpfennig, I., Ermini, M., ASTER Team, 2017. ^{10}Be exposure dating of the timing of Neoglacial glacier advances in the Ecrins-Pelvoux massif, southern French Alps. Quat. Sci. Rev. 178, 118–138. https://doi.org/10.1016/j.quascirev.2017.10.010.
Lehmann, B., Herman, F., Valla, P.G., King, G.E., Biswas, R.H., Ivy-Ochs, S., Steinemann, O., Christl, M., 2020. Postglacial erosion of bedrock surfaces and deglaciation timing: new insights from the Mont Blanc massif (western Alps). Geology 48, 139–144. https://doi.org/10.1130/G46585.1.
Li, H., Spötl, C., Cheng, H., 2021. A high-resolution speleothem proxy record of the Late Glacial in the European Alps: extending the NALPS19 record until the beginning of the Holocene. J. Quat. Sci. 36, 29–39. https://doi.org/10.1002/jqs.3255.
Lifton, N., 2016. Implications of two Holocene time-dependent geomagnetic models for cosmogenic nuclide production rate scaling. Earth Planet Sci. Lett. 433, 257–268. https://doi.org/10.1016/J.EPSL.2015.11.006.
Lifton, N., Sato, T., Dunai, T.J., 2014. Scaling in situ cosmogenic nuclide production rates using analytical approximations to atmospheric cosmic-ray fluxes. Earth Planet Sci. Lett. 386, 149–160. https://doi.org/10.1016/J.EPSL.2013.10.052.
Lotter, A.F., Eicher, U., Siegenthaler, U., Birks, H.J.B., 1992. Late-glacial climatic oscillations as recorded in Swiss lake sediments. J. Quat. Sci. 7, 187–204. https://doi.org/10.1002/jqs.3390070302.
Lovell, H., Fleming, E.J., Benn, D.I., Hubbard, B., Lukas, S., Naegeli, K., 2015. Former dynamic behaviour of a cold-based valley glacier on Svalbard revealed by basal ice and structural glaciology investigations. J. Glaciol. 61, 309–328. https://doi.org/10.3189/2015JoG14J120.
Lowell, T.V., 1995. The application of radiocarbon age estimates to the dating of glacial sequences: an example from the Miami sublobe, Ohio. U.S.A. Quat. Sci. Rev. 14, 85–99. https://doi.org/10.1016/0277-3791(94)00113-.
Lowick, S.E., Buechi, M.W., Gaar, D., Graf, H.R., Preusser, F., 2015. Luminescence dating of Middle Pleistocene proglacial deposits from northern Switzerland: methodological aspects and stratigraphical conclusions. Boreas 44, 459–482. https://doi.org/10.1111/bor.12114.
Luetscher, M., Boch, R., Sodemann, H., Spötl, C., Cheng, H., Edwards, R.L., Frisia, S., Hof, F., Müller, W., 2015. North Atlantic storm track changes during the last glacial maximum recorded by alpine speleothems. Nat. Commun. 6. https://doi.org/10.1038/ncomms7344.
Lukas, S., 2012. Processes of annual moraine formation at a temperate alpine valley glacier: insights into glacier dynamics and climatic controls. Boreas 41 (3), 463–480. https://doi.org/10.1111/j.1502-3885.2011.00241.x.
Mackintosh, A.N., Anderson, B.M., Pierrehumbert, R.T., 2017. Reconstructing climate from glaciers. Annu. Rev. Earth Planet Sci. 45, 649–680. https://doi.org/10.1146/annurev-earth-063016-020643.
Martin, L.C.P., Blard, P.-H., Balco, G., Lavé, J., Delunel, R., Lifton, N., Laurent, V., 2017. The CREp program and the ICE-D production rate calibration database: a fully parameterizable and updated online tool to compute cosmic-ray exposure ages. Quat. Geochronol. 38, 25–49. https://doi.org/10.1016/J.QUAGEO.2016.11.006.
McColl, S.T., 2012. Paraglacial rock-slope stability. Geomorphology 153–154, 1–16. https://doi.org/10.1016/J.GEOMORPH.2012.02.015.
Merchel, S., Herpers, U., 1999. An update on radiochemical separation techniques for the determination of long-lived radionuclides via accelerator mass spectrometry. Radiochim. Acta 84. https://doi.org/10.1524/ract.1999.84.4.215.
Mey, J., D'Arcy, M.K., Schildgen, T.F., Egholm, D.L., Wittmann, H., Strecker, M.R., 2020. Temperature and precipitation in the southern central andes during the last glacial maximum, Heinrich stadial 1, and the younger Dryas. Quat. Sci. Rev. 248, 106592. https://doi.org/10.1016/j.quascirev.2020.106592.
Mey, J., Scherler, D., Wickert, A.D., Egholm, D.L., Tesauro, M., Schildgen, T.F., Strecker, M.R., 2016. Glacial isostatic uplift of the European Alps. Nat. Commun. 7, 1–10. https://doi.org/10.1038/ncomms13382.
Monegato, G., Scardia, G., Hajdas, I., Rizzini, F., Piccin, A., 2017. The Alpine LGM in the boreal ice-sheets game. Sci. Rep. 7 (1), 1–8.
Nesje, A., 1992. Topographical effects on the equilibrium-line altitude on glaciers. Geojournal 27 (4), 383–391.
Nicolussi, K., Schlüchter, C., 2012. The 8.2 ka event-Calendar-dated glacier response in the Alps. Geology 40, 819–822. https://doi.org/10.1130/G32406.1.
Nicoud, G., De Los Cobos, G., Fudral, S., Dray, M., Pollicini, F., Novel, J.P., Parriaux, A., Zuppi, G.M., Bonetto, F., Paillet, A., Olive, P., Puig, J.M., 1999. Les etapes du comblement alluvial de la plaine d'Aoste (Italie): une dynamique lacustre complexe. Eclogae Geol. Helv. 92, 139–147.
Oerlemans, J., 2005. Atmospheric science: extracting a climate signal from 169 glacier records. Science 308, 675–677. https://doi.org/10.1126/science.1107046.
Osmaston, H., 2005. Estimates of glacier equilibrium line altitudes by the Area× altitude, the Area× altitude balance ratio and the Area× altitude balance index methods and their validation. Quat. Int. 138, 22–31. https://doi.org/10.1016/j.quaint.2005.02.004.
Pánek, T., Břežný, M., Kilnar, J., Winocur, D., 2021. Complex causes of landslides after ice sheet retreat: post-LGM mass movements in the Northern Patagonian Icefield region. Sci. Total Environ. 758, 143684. https://doi.org/10.1016/j.scitotenv.2020.143684.
Pellitero, R., Rea, B.R., Spagnolo, M., Bakke, J., Hughes, P., Ivy-Ochs, S., Lukas, S.,

Ribolini, A., 2015. A GIS tool for automatic calculation of glacier equilibrium-line altitudes. Comput. Geosci. 82, 55–62. https://doi.org/10.1016/j.cageo.2015.05.005.
Pellitero, R., Rea, B.R., Spagnolo, M., Bakke, J., Ivy-Ochs, S., Frew, C.R., Hughes, P., Ribolini, A., Lukas, S., Renssen, H., 2016. GlaRe, a GIS tool to reconstruct the 3D surface of palaeoglaciers. Comput. Geosci. https://doi.org/10.1016/j.cageo.2016.06.008.
Perello, P., Gianotti, F., Monopoli, B., 2008. Carta Geologica d'Italia - Foglio 089. Courmayeur.
Polino, R., Malusà, M.G., Martin, S., Carraro, F., Gianotti, F., Bonetto, F., 2008. Carta Geologica d'Italia - Foglio 090 (Aosta).
Porter, S.C., Orombelli, G., 1982. Late-glacial ice advances in the western Italian Alps. Boreas 11, 125–140. https://doi.org/10.1111/j.1502-3885.1982.tb00530.x.
Porter, S.C., Orombelli, G., 1985. Glacier contraction during the middle Holocene in the western Italian Alps: evidence and implications. Geology 13 (4), 296–298. https://doi.org/10.1130/0091-7613(1985)13<296:GCDTMH>2.0.CO;2.
Preusser, F., Kasper, H.U., 2001. Comparison of dose rate determination using high-resolution gamma spectrometry and inductively coupled plasma-mass spectrometry. Anc. TL 19, 17–21.
Protin, M., Schimmelpfennig, I., Mugnier, J.L., Ravanel, L., Le Roy, M., Deline, P., Favier, V., Buoncristiani, J.F., Aumaître, G., Bourlès, D.L., Keddadouche, K., 2019. Climatic reconstruction for the younger dryas/early Holocene transition and the Little ice age based on paleo-extents of argentière glacier (French Alps). Quat. Sci. Rev. 221. https://doi.org/10.1016/j.quascirev.2019.105863.
Rasmussen, S.O., Bigler, M., Blockley, S.P., Blunier, T., Buchardt, S.L., Clausen, H.B., Cvijanovic, I., Dahl-Jensen, D., Johnsen, S.J., Fischer, H., Gkinis, V., Guillevic, M., Hoek, W.Z., Lowe, J.J., Pedro, J.B., Popp, T., Seierstad, I.K., Steffensen, J.P., Svensson, A.M., Vallelonga, P., Vinther, B.M., Walker, M.J.C., Wheatley, J.J., Winstrup, M., 2014. A stratigraphic framework for abrupt climatic changes during the Last Glacial period based on three synchronized Greenland ice-core records: refining and extending the INTIMATE event stratigraphy. Quat. Sci. Rev. 106, 14–28. https://doi.org/10.1016/j.quascirev.2014.09.007.
Rasmussen, S.O., Vinther, B.M., Clausen, H.B., Andersen, K.K., 2007. Early Holocene climate oscillations recorded in three Greenland ice cores. Quat. Sci. Rev. 26, 1907–1914. https://doi.org/10.1016/j.quascirev.2007.06.015.
Ravazzi, C., Pini, R., Badino, F., De Amicis, M., Londeix, L., Reimer, P.J., 2014. The latest LGM culmination of the Garda Glacier (Italian Alps) and the onset of glacial termination. Age of glacial collapse and vegetation chronosequence. Quat. Sci. Rev. 105, 26–47. https://doi.org/10.1016/j.quascirev.2014.09.014.
Rea, B.R., Pellitero, R., Spagnolo, M., Hughes, P., Ivy-Ochs, S., Renssen, H., Ribolini, A., Bakke, J., Lukas, S., Braithwaite, R.J., 2020. Atmospheric circulation over europe during the younger Dryas. Sci. Adv. 6 (50), 4844. https://doi.org/10.1126/sciadv.aba4844.
Regattieri, E., Zanchetta, G., Isola, I., Zanella, E., Drysdale, R.N., Hellstrom, J.C., Zerboni, A., Dallai, L., Tema, E., Lanci, L., Costa, E., Magrì, F., 2019. Holocene Critical Zone dynamics in an Alpine catchment inferred from a speleothem multiproxy record: disentangling climate and human influences. Sci. Rep. 9, 1–9. https://doi.org/10.1038/s41598-019-53583-7.
Regione Autonoma Valle d'Aosta, 2009. RENDICONTO IDRO-METEOROLOGICO 2000-2009 Pioggia, temperatura, neve e dissesti 10 anni di dati.
Reimann, T., Tsukamoto, S., 2012. Dating the recent past (<500 years) by post-IR IRSL feldspar - examples from the north sea and baltic sea coast. Quat. Geochronol. 10, 180–187. https://doi.org/10.1016/j.quageo.2012.04.011.
Reitner, J.M., 2007. Glacial dynamics at the beginning of Termination I in the Eastern Alps and their stratigraphic implications. Quat. Int. 164–165, 64–84. https://doi.org/10.1016/j.quaint.2006.12.016.
Reixach, T., Delmas, M., Braucher, R., Gunnell, Y., Mahé, C., Calvet, M., 2021. Climatic conditions between 19 and 12 ka in the eastern Pyrenees, and wider implications for atmospheric circulation patterns in Europe. Quat. Sci. Rev. 260, 106923. https://doi.org/10.1016/j.quascirev.2021.106923.
Rolland, Y., Darnault, R., Braucher, R., Bourlès, D., Petit, C., Bouissou, S., ASTER Team, 2020. Deglaciation history at the Alpine-Mediterranean transition (Argentera-Mercantour, SW Alps) from ^{10}Be dating of moraines and glacially polished bedrock. Earth Surf. Process. Landforms 45 (2), 393–410. https://doi.org/10.1002/esp.4740.
Samartin, S., Heiri, O., Vescovi, E., Brooks, S.J., Tinner, W., 2012. Lateglacial and early Holocene summer temperatures in the southern Swiss Alps reconstructed using fossil chironomids. J. Quat. Sci. 27, 279–289. https://doi.org/10.1002/jqs.1542.
Sanchez, G., Rolland, Y., Corsini, M., Braucher, R., Bourlès, D., Arnold, M., Aumaître, G., 2010. Relationships between tectonics, slope instability and climate change: cosmic ray exposure dating of active faults, landslides and glacial surfaces in the SW Alps. Geomorphology 117 (1–2), 1–13. https://doi.org/10.1016/j.geomorph.2009.10.019.
Schimmelpfennig, I., Schaefer, J.M., Akçar, N., Ivy-Ochs, S., Finkel, R.C., Schlüchter, C., 2012. Holocene glacier culminations in the Western Alps and their hemispheric relevance. Geology 40, 891–894. https://doi.org/10.1130/G33169.1.
Schimmelpfennig, I., Schaefer, J.M., Akçar, N., Koffman, T., Ivy-Ochs, S., Schwartz, R., Finkel, R.C., Zimmerman, S., Schlüchter, C., 2014. A chronology of Holocene and Little Ice Age glacier culminations of the Steingletscher, Central Alps, Switzerland, based on high-sensitivity beryllium-10 moraine dating. Earth Planet Sci. Lett. 393, 220–230. https://doi.org/10.1016/j.epsl.2014.02.046.
Schindelwig, I., Akçar, N., Kubik, P.W., Schlüchter, C., 2012. Lateglacial and early Holocene dynamics of adjacent valley glaciers in the Western Swiss Alps. J. Quat. Sci. 27, 114–124. https://doi.org/10.1002/jqs.1523.
Schmidt, R., Weckström, K., Lauterbach, S., Tessadri, R., Huber, K., 2012. North Atlantic climate impact on early late-glacial climate oscillations in the south-eastern Alps inferred from a multi-proxy lake sediment record. J. Quat. Sci. 27, 40–50. https://doi.org/10.1002/jqs.1505.
Schwartz, S., Zerathe, S., Jongmans, D., Baillet, L., Carcaillet, J., Audin, L., Dumont, T., Bourlès, D., Braucher, R., Lebrouc, V., 2017. Cosmic ray exposure dating on the large landslide of Séchilienne (Western Alps): a synthesis to constrain slope evolution. Geomorphology 278, 329–344. https://doi.org/10.1016/j.geomorph.2016.11.014.
Seguinot, J., Ivy-Ochs, S., Jouvet, G., Huss, M., Funk, M., Preusser, F., 2018. Modelling last glacial cycle ice dynamics in the Alps. Cryosphere 12, 3265–3285. https://doi.org/10.5194/tc-12-3265-2018.
Serra, E., Valla, P.G., Gribenski, N., Guedes Magrani, F., Carcaillet, J., Delaloye, R., Grobéty, B., Braillard, L., 2021. Geomorphic response to the lateglacial–holocene transition in high alpine regions (sanetsch pass, Swiss Alps). Boreas 50 (1), 242–261. https://doi.org/10.1111/bor.12480.
Smedley, R.K., Glasser, N.F., Duller, G.A.T., 2016. Luminescence dating of glacial advances at lago buenos aires (~46 °S), patagonia. Quat. Sci. Rev. 134, 59–73. https://doi.org/10.1016/j.quascirev.2015.12.010.
Spagnolo, M., Ribolini, A., 2019. glacier extent and climate in the maritime Alps during the younger Dryas. Palaeogeogr. Palaeoclimatol. Palaeoecol. 536, 109400. https://doi.org/10.1016/j.palaeo.2019.109400.
Stanford, J.D., Rohling, E.J., Bacon, S., Roberts, A.P., Grousset, F.E., Bolshaw, M., 2011. A new concept for the paleoceanographic evolution of Heinrich event 1 in the North Atlantic. Quat. Sci. Rev. 30, 1047–1066. https://doi.org/10.1016/j.quascirev.2011.02.003.
Tinner, W., Lotter, A.F., 2001. Central European vegetation response to abrupt climate change at 8.2 ka. Geology 29, 551–554. https://doi.org/10.1130/0091-7613(2001)029<0551:CEVRTA>2.0.CO;2.
Turrin, J.B., Forster, R.R., Sauber, J.M., Hall, D.K., Bruhn, R.L., 2014. Effects of bedrock lithology and subglacial till on the motion of Ruth Glacier, Alaska, deduced from five pulses from 1973 to 2012. J. Glaciol. 60, 771–781. https://doi.org/10.3189/2014JoG13J182.
Uppala, S.M., Källberg, P.W., Simmons, A.J., Andrae, U., da Costa Bechtold, V., Fiorino, M., Gibson, J.K., Haseler, J., Hernandez, A., Kelly, G.A., Li, X., Onogi, K., Saarinen, S., Sokka, N., Allan, R.P., Andersson, E., Arpe, K., Balmaseda, M.A., Beljaars, A.C.M., van de Berg, L., Bidlot, J., Bormann, N., Caires, S., Chevallier, F., Dethof, A., Dragosavac, M., Fisher, M., Fuentes, M., Hagemann, S., Hólm, E., Hoskins, B.J., Isaksen, L., Janssen, P.A.E.M., Jenne, R., McNally, A.P., Mahfouf, J.F., Morcrette, J.J., Rayner, N.A., Saunders, R.W., Simon, P., Sterl, A., Trenberth, K.E., Untch, A., Vasiljevic, D., Viterbo, P., Woollen, J., 2005. The ERA-40 re-analysis. Q. J. R. Meteorol. Soc. 131, 2961–3012. https://doi.org/10.1256/qj.04.176.
Vanuzzo, C., 2001. The glacier retreat in Valle D'Aosta (Western Italian Alps) from the Little Ice Age to the second half of the 20th century: linear, areal, volumetric and equilibrium line altitute changes. Geogr. Fis. Din. Quaternaria 24, 99–113.
Vezzoli, G., Garzanti, E., Monguzzi, S., 2004. Erosion in the western Alps (Dora Baltea basin). 1. Quantifying sediment provenance. Sediment. Geol. 171, 227–246. https://doi.org/10.1016/j.sedgeo.2004.05.017.
Viani, C., Machguth, H., Huggel, C., Godio, A., Franco, D., Perotti, L., Giardino, M., 2020. Potential future lakes from continued glacier shrinkage in the Aosta valley region (western Alps, Italy). Geomorphology 355, 107068. https://doi.org/10.1016/j.geomorph.2020.107068.
Višnjević, V., Herman, F., Prasicek, G., 2020. Climatic patterns over the European Alps during the LGM derived from inversion of the paleo-ice extent. Earth Planet Sci. Lett. 538, 116185.
Von Grafenstein, U., Erlenkeuser, H., Brauer, A., Jouzel, J., Johnsen, S.J., 1999. A mid-European decadal isotope-climate record from 15,500 to 5000 years B.P. Science 284, 1654–1657. https://doi.org/10.1126/science.284.5420.1654.
Wirsig, C., Zasadni, J., Christl, M., Akçar, N., Ivy-Ochs, S., 2016a. Dating the onset of LGM ice surface lowering in the High Alps. Quat. Sci. Rev. 143, 37–50. https://doi.org/10.1016/j.quascirev.2016.05.001.
Wirsig, C., Zasadni, J., Ivy-Ochs, S., Christl, M., Kober, F., Schlüchter, C., 2016b. A deglaciation model of the Oberhasli, Switzerland. J. Quat. Sci. 31, 46–59. https://doi.org/10.1002/jqs.2831.
Zerathe, S., Lebourg, T., Braucher, R., Bourlès, D., 2014. Mid-Holocene cluster of large-scale landslides revealed in the Southwestern Alps by ^{36}Cl dating. Insight on an Alpine-scale landslide activity. Quat. Sci. Rev. 90, 106–127. https://doi.org/10.1016/j.quascirev.2014.02.015.